npj computational materials

www.nature.com/npjcompumats

REVIEW ARTICLE OPEN

Enhancing the Faradaic efficiency of solid oxide electrolysis cells: progress and perspective

Prashik S. Gaikwad[1], Kunal Mondal[1], Yun Kyung Shin[2], Adri C. T. van Duin[2] and Gorakh Pawar[1]✉

To reduce global warming, many countries are shifting to sustainable energy production systems. Solid oxide electrolysis cells (SOECs) are being considered due to their high hydrogen generation efficiency. However, low faradaic efficiency in scaling SOEC technology affects costs and limits large-scale adoption of hydrogen as fuel. This review covers SOECs' critical aspects: current state-of-the-art anode, cathode, and electrolyte materials, operational and materials parameters affecting faradaic efficiency, and computational modeling techniques to resolve bottlenecks affecting SOEC faradaic efficiency.

npj Computational Materials (2023)9:149 ; https://doi.org/10.1038/s41524-023-01044-1

INTRODUCTION

During the Industrial Revolution, overdependence and over-utilization of fossil fuels led to an increase in greenhouse gas (GHG) emissions, such as carbon dioxide, methane, etc. Due to this increase, the average global temperature also has increased by 1.2 °C since 1880—with the greatest changes coming in just the late twentieth century[1]. In order to tackle this issue, many countries are reviewing energy transition strategies to shift towards carbon neutrality[1,2]. For instance, almost all members of the United Nations signed the Paris Agreement in 2016 to keep the average global temperature rise to below 2 °C by 2100 as compared with pre-industrial levels and pursue efforts to limit this increase to just 1.5 °C[3]. Consequently, many countries are transitioning towards clean and low-carbon energy to promote decarbonization[1].

Hydrogen (H_2) has received significant attention as a clean energy carrier from both researchers[4] and policy makers[5], and is an important part of the energy mix in a low-carbon energy future[6]. Green H_2 is the cleanest form of H_2 with zero carbon emissions, which is produced using renewable energy[1]. An increased use of renewable energy is important to achieve a sustainable green H_2[7]. Currently, renewable energy H_2 production technologies include water electrolysis and biogas steam reforming. Electrolysis using wind- or hydro-generated electricity is considered to be one of the best green H_2 production sources[8]. Electrolysis can be performed using three types of electrolysis cells: (1) alkaline electrolysis cells (AECs); (2) proton exchange membrane (PEM) electrolysis cells; and (3) solid oxide electrolysis cells (SOECs)[9]. Among these, SOECs can generate H_2 with the highest efficiency[10–12]. Despite the merits of SOECs, the major drawbacks in scaling SOEC technology are their low faradaic efficiency and high energy costs—or costs per kilogram of H_2—that limit the large-scale adoption of H_2 as a fuel.

This current review focuses on various operating and materials factors affecting the faradaic efficiency of SOECs, the recent advances in the computational materials science aimed to model various SOEC intrinsic processes, and the needed future computational developments that would complement the ongoing experimental efforts and generate new ground-breaking knowledge required to improve the SOEC faradaic efficiency. In particular, SOEC electrolyte materials are investigated deeply.

MATERIALS USED IN THE SOECS

In this section, the state-of-the-art materials for electrodes (e.g., cathode and anode) and electrolytes (e.g., oxygen-ion conducting and proton-ion conducting) are reviewed. The first subsection describes the advanced electrode materials, while the second subsection provides an update on recent developments in common electrolyte materials.

Electrodes

In SOECs, the selection of two electrodes—anodes and cathodes—is a vital parameter in determining the overall performance of H_2 gas production. Electrodes in SOECs should have the following properties: (a) high ionic conductivity for allowing geometric extension of reaction zone in the entire volume of electrode; (b) high electronic conductivity to improve collection of electrons; (c) a highly porous microstructure for promoting the diffusion of gas, which is a fundamental parameter for oxidation/reduction reactions that ultimately results in increasing the efficiency of SOECs; and (d) high catalytic activity. The active reaction site occurs at the triple-phase boundary, which is the interface between the electronic conductor, the ionic conductor, and the gas diffusion pore[10–12].

The most common cathode materials that are used in SOECs are nickel (Ni)-based composite materials with yttria (Y_2O_3)-stabilized zirconia (ZrO_2) (YSZ) and yttrium (Y)-doped barium cerate zirconate (BCZY)[10–12]. The main advantages in using Ni-based cathode electrodes are their high electronic conductivity, that they are excellent reforming catalysts, and that they are an electro-catalyst for the electrochemical reduction of water. The Ni-composite electrode acts as a fabrication of supported cell geometry, which allows for the formation of a thin electrolyte, a reduction in ohmic losses, lowering the activation potential, and promoting the electrochemical activity during SOEC operation. Cathode electrode materials are chosen based on the following properties: (1) optimal properties at high temperatures; (2) chemical stability in reducing atmosphere; and (3) a minimal

[1]Department of Material Science and Manufacturing Engineering, Idaho National Laboratory, Idaho Falls, ID 83415, USA. [2]Department of Mechanical Engineering, Pennsylvania State University, University Park, PA 16802, USA. ✉email: gorakh.pawar@inl.gov

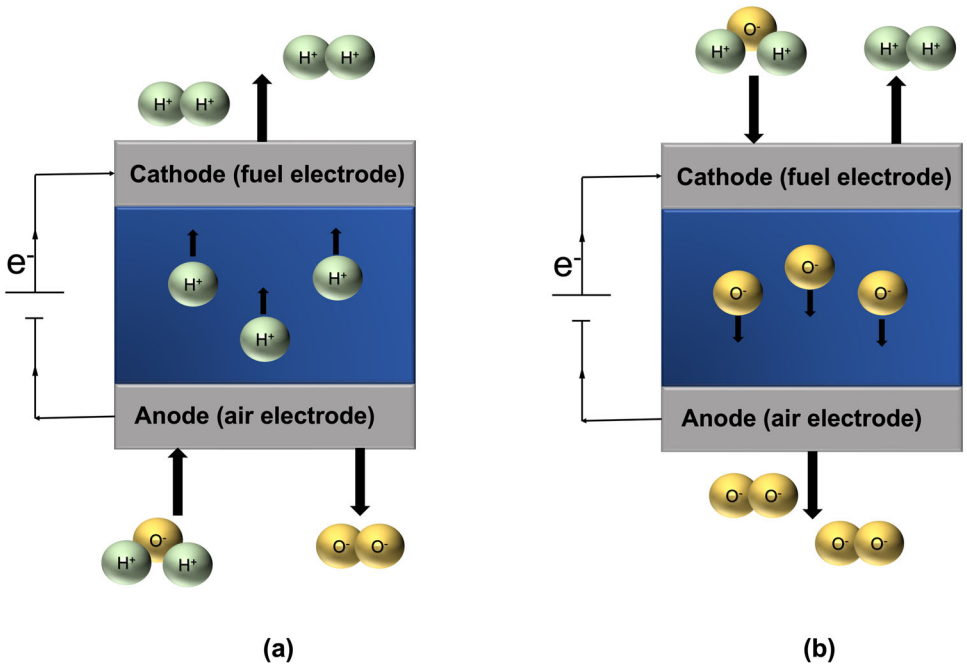

Fig. 1 Schematic diagrams of types of electrolytes used in SOECs. a A proton-ion conducting electrolyte; and **b** an oxygen-ion conducting electrolyte.

mismatch of thermal and chemical expansion coefficients relative to those of the electrolyte material to prevent mechanical stress. Despite the investigation of different cathode materials, no material exists to meet all of these requirements. One of the most promising strategies for improving stability and electrochemical catalytic activity is the addition of doping materials like manganese (Mn), neodymium (Nd), iron (Fe), and chromium (Cr).

Commonly used anode materials are perovskite (ABO_3)-based materials[10–12]. The A-site is occupied by large trivalent lanthanide ions (e.g., La^{3+}, Pr^{3+}, Sm^{3+}, Gd^{3+}) and is substituted by divalent alkali earth ions (e.g., Ca^{2+}, Sr^{2+}, Ba^{2+}) in order to increase the electronic and ionic conductivities[13]. The B-site is substituted by small trivalent or tetravalent three-dimensional (3D) transition metal ions (e.g., $Mn^{3+/4+}$, $Fe^{3+/4+}$, $Co^{3+/4+}$, $Ni^{3+/4+}$). Strontium-based lanthanum manganite (LSM) is the most commonly used anode electrode material. LSM has a thermal expansion coefficient close to one of the electrolytes, which stabilizes the cell mechanism. LSM is known to have a high electronic conductivity, but a poor ionic conductivity. Other perovskite-based materials—such as double-perovskites and Ruddlesden-Popper (RP)-based materials—also are widely used as anode electrode materials due to their high potential stability and improved performance under a redox atmosphere. The RP-based materials show a higher oxygen-ion conductivity than regular perovskite materials[10–12]. In double-layered perovskite materials (e.g., $AA_0B_2O_{5+\delta}$), the A-site is normally occupied by a trivalent lanthanide ion and the A_0-site by barium (Ba) or strontium (Sr), while the B-site is a mixture of the first-row transition metal ions.

Electrolytes

The most important electrochemical system component is the electrolyte. It has a large impact on cell performance through its contribution to the ohmic internal resistance. The ideal electrolyte used in SOECs should possess a high ionic conductivity, a negligible electronic conductivity, a good thermal and chemical stability, a matching thermal coefficient, a lower activation energy, a high density, and a minimum reactant crossover[13].

SOECs can be further subdivided into two categories—oxygen-ion conducting cells and proton-ion conducting cells, as shown in Fig. 1. The most distinct difference between the proton-ion and oxygen-ion SOEC is the electrolyte-conducting ion, which further results in different working principles. In the case of the proton-ion conducting electrolyte, H^+ ions/protons are transported from the anode electrode to the cathode electrode, where H_2 gas is produced. In the case of the oxide-ion conducting electrolyte, the oxygen ions migrate from the cathode side of the cell to the anode side. Steam is fed to the anode side in the case of the proton-ion conducting electrolyte; however, for the oxygen-ion electrolyte, it is fed to the cathode side. There are several advantages of using a proton-ion electrolysis cell, such as dry and pure H_2 gas that can be directly produced at the cathode side of the fuel, which further simplifies the system and reduces operational costs. Compressed H_2 can be directly produced through increasing the operating pressure. Thus, in-situ electrochemical compression can potentially increase the total energy efficiency[14]. The operating temperature of the proton-ion electrolysis cell is around 673 to 973 K, which is lower than that of the oxygen-ion electrolysis cell of 973 to 1273 K. The lower operating temperature leads to a lower cost in sealing materials and interconnection, which increases the overall durability of the cell. A detailed description of the different oxygen-ion and proton-ion electrolyte materials is provided in ref. [15].

Oxygen-ion conductivity arises due to the mobility of oxygen point defects, which can be oxygen vacancies or the transport of oxygen in the positions of the interstitials via a hopping mechanism[16]. Zirconia- and ceria-based materials are widely investigated as potential candidates for the oxygen-ion conducting electrolyte. In the case of ceria-based material, partial electronic conductivity at elevated temperatures and a reduced atmosphere occurs, which is due to the reduction of the Ce^{4+} to Ce^{3+} ions. Such partial electronic conductivity causes a decrease in faradaic efficiency[17]. YSZ is commonly used as an oxygen-ion conducting electrolyte because it can be used in high temperature applications[16]. YSZ is developed by using cubic fluorite structure yttria (Y_2O_3) as a dopant within the zirconia (ZrO_2) structure. Despite having excellent conductivity during SOEC operation, the degradation of material and a reduction in the performance of SOEC hindered the further investigation and development of YSZ

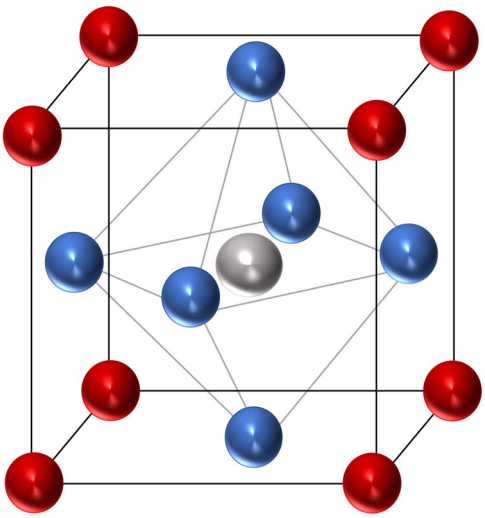

Fig. 2 A typical Perovskite crystal structure. In a Perovskite crystal structure (ABO_3), red spheres represent A-site cations, the grey sphere is the B-site cation, and the blue spheres are oxygen ions.

material. The degradation issues and low ionic conductivity of YSZ has led to the development of scandia (Sc_2O_3)-stabilized zirconia (ScSZ) material, which shows higher ionic conductivity than YSZ at intermediate temperatures. In addition, the current density of ScSZ-based electrolytes is approximately twice that of the YSZ-based electrolytes[18]. However, the cost of Sc in addition to small Sc ion size would lead to diffusivity and separation into impurity phases[19]. $LaGaO_3$-based materials have shown high conductivity and a high transfer number of O^{2-} ions, thus making them a promising electrolyte candidate at intermediate temperatures[18]. However, the incompatibility of the Ni-based cathode and $LaGaO_3$-based electrolyte is a major issue in $LaNiO_3$ formation[20].

In summary, due to the high operating temperatures of oxygen-ion conducting electrolytes, the degradation of the cell occurs at a faster rate. Even the current state-of-the-art YSZ oxygen-ion conducting electrolyte suffers degradation in the high corrosive environment of electrolysis and shows a lower ion conductivity and lower catalytic activity at lower operating temperatures[17]. Most of the delamination failure occurs at the interface region between the cathode electrode and the electrolyte, which is primarily caused due to the mismatch of the thermal expansion coefficient of the materials[20]. For this reason, the trend has shifted towards the proton-ion conducting electrolyte materials, which offer more advantages as mentioned earlier.

Due to their easy synthesis, high thermal stability, and low cost, perovskite crystal structure (ABO_3)-based proton-ion conducting electrolytes, as observed in Fig. 2[21], have gained more attention than fluorite (AO_2) and pyrochlore ($A_2B_2O_7$)-based electrolytes[22]. In a typical perovskite structure, the A-site is occupied by an alkaline-earth element (e.g., Ba, Sr, Ca), while the B-site is occupied by a tetravalent element—usually Ce or Zr. For an electrolyte, protonation is required, which increases the number of charge carriers while still keeping the material neutral. Thus, to promote protonic conductivity, it is important to dope the B-site with trivalent elements (e.g., Y, Nd, Sm, Yb, In, Eu, Gd, etc.). Doping with trivalent elements leads to the formation of oxygen vacancies that play a crucial part in the formation and mobility of protons. Protons are transported through three major steps: (1) dissociative adsorption; (2) Grotthuss mechanism; and (3) rotational diffusion. With dissociative adsorption, oxygen defects are created after the addition of trivalent elements to keep a neutral charge in the system. For every two dopant atoms, one oxygen vacancy is created. In the presence of water vapor, these oxygen vacancies are occupied by the hydroxyl ions that are formed by dissociation

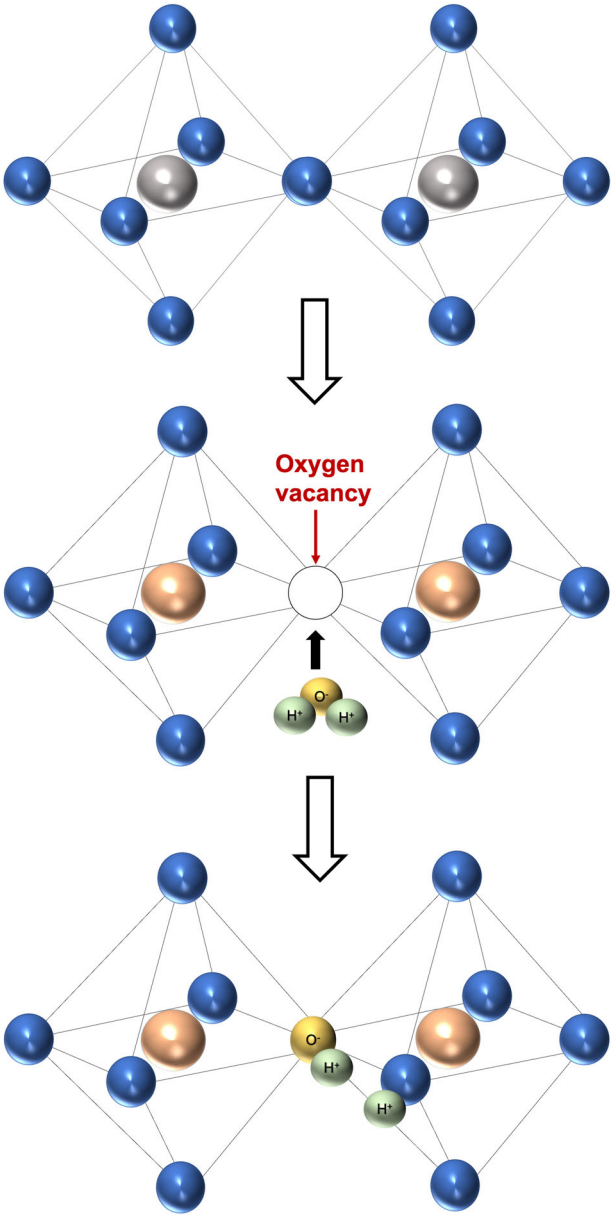

Fig. 3 Schematic representation of protonation process in perovskite-type materials. Blue sphere represents oxygen ions, grey spheres are the B-site cations, and orange-colored spheres are the doping elements.

of water into H_2 (protons) and hydroxide ions, as shown in Fig. 3. With the Grotthuss mechanism, the mobile protons or the H_2 ions interact to form a weak bond with oxygen atoms, as seen in Fig. 4. With rotational diffusion, the protonic defect rotates and reorients itself to facilitate the transport of protons from one oxygen atom to the neighboring oxygen atom[16], as shown in Fig. 4.

The most commonly investigated proton-ion conducting electrolyte materials are barium cerate ($BaCeO_3$) and barium zirconate ($BaZrO_3$). Among these two materials, $BaCeO_3$ has a high proton conductivity[23–25]; however, it also has a low chemical stability, which makes it unsuitable for applications. On the other hand, barium zirconate-based electrolytes exhibit good chemical stability under carbon dioxide and a water-containing atmosphere. However, due to the refractory nature of $BaZrO_3$, high sintering temperatures (e.g., >1600 °C) are required, which makes the fabrication of this material highly unfeasible.

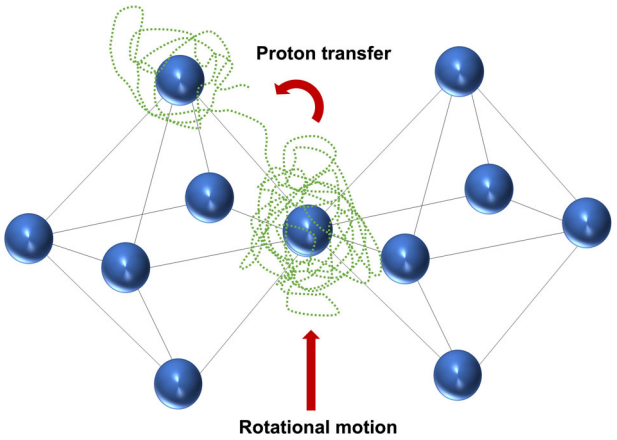

Fig. 4 Schematic representation of protonation process in perovskite-type materials. (Adapted with permission from ref. [15] under Copyright Clearance Center Inc).

In general, further research and developments in proton-ion conducting electrolytes can make the ideal choice as the electrolyte materials, which will have high ionic conductivity, negligible electronic conductivity, and good thermal and chemical stability.

FACTORS AFFECTING THE EFFICIENCY OF SOEC

A much-desired electrolyte material property is negligible electronic conductivity. Unfortunately, non-negligible charge carriers—other than protons—are known to exist[26–29]. Fig. 5 schematically illustrates the charge carriers in a proton-ion conducting electrolyte. The existence of partial charge carriers—such as an oxide-ion, hole, and electron—decreases the protonic transfer number and overall efficiency of the cell. In the oxidizing environment, the formation of electron holes occurs, and the presence of holes causes the internal leakage current, which further results in a decrease of the faradaic efficiency[29–32].

Iwahara et al.[33] reported that the faradaic efficiency of the proton-ion conducting electrolyte is between 50 and 95%. Babiniec et al.[34] measured a faradaic efficiency of only 32% at 100 mA and 973 K for the cell having a thin BCZY27 electrolyte layer and a Ni-BCZY27 fuel electrode. Using BZY20 as the electrolyte material, the faradaic efficiency ~63.6% at 1.3 V and 873 K was reported by Lei et al.[35] Details of more faradaic efficiencies with a variety of electrode and electrolyte materials can be found elsewhere[36]. Low faradaic efficiency decreases the overall performance of the electrolysis cell. In order to tackle this issue, studying different factors influencing the efficiency is paramount.

An important factor in increasing faradaic efficiency is to reduce the electronic conductivity of the electrolyte material. The effects of temperature, O_2 partial pressure, H_2O partial pressure, chemical composition, and external current (externally applied voltage) on the electronic conductivity have been studied thoroughly in the literature[32]. In addition to the above factors, additional strategies are discussed that help in increasing the faradaic efficiencies.

Temperature

The activation energy for the electronic conductivity is greater than the oxygen-ionic and protonic conductivities[37,38]. Thus, as the temperature increases, a significant increase in the electronic conductivity is observed. To reduce the unwanted effects of electronic contribution, lowering the operational temperature of the electrolysis cell can be the best option to consider[39]. This strategy is an ongoing process by developing new electrolyte materials[38,40–42], novel thin film technologies[43–45], and an innovative highly active electrode system[46–48]. It has been demonstrated theoretically and experimentally that decreasing the operating temperature decreases the electronic conductivity for BZY, BCZY, and BCY materials[39,49]. In addition, lowering the operational temperature helps in maintaining the low ohmic resistance of the electrolyte and low polarization resistance of the electrode.

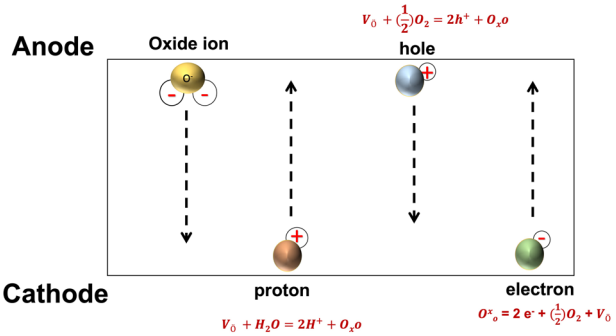

Fig. 5 A schematic representation on the existence of partial charge carriers.

Water and oxygen partial pressure

Under humidifying atmosphere, protons are formed due to the dissociation of water. The oxygen vacancies ($V_{\ddot{o}}$) that were previously generated by acceptor doping are occupied by the hydroxide ion, thereby forming a protonic defect ($OH_{\dot{o}}$) which leads to the formation of a weak bond between proton and the regular lattice oxide-ion, as observed in Fig. 2. The hydration reaction is as follows[32,50]:

$$H_2O + V_{\ddot{o}} + O_x^o \leftrightarrows 2OH_{\dot{o}} \quad (1)$$

While in an oxidizing atmosphere, the oxygen occupies the $V_{\ddot{o}}$, which leads to the appearance of electronic holes ($\dot{h}$). The redox reaction is as follows[32,50]:

$$0.5\,O_{2,gas} + V_{\ddot{o}} \leftrightarrows O_x^o + 2\dot{h} \quad (2)$$

Heras-Juaristi et al.[49] investigated the partial conductivity of oxygen-ion (σ_v), proton (σ_H) and electron hole (σ_h) as a function of partial pressure of water (pH_2O) in the BCZY27 material, as observed in Fig. 6. At high temperature (800 °C) and high partial pressure of oxygen ($pO_2 = 0.2$ atm), as shown in Fig. 6a, σ_h was the main contributor towards the total conductivity (σ_{total}) of the material. While at lower pO_2 (~10^{-5} atm), as seen in Fig. 6b, the contribution of σ_h towards the σ_{total} decreases. This means that the high pO_2 leads to larger electronic conductivity, which can be explained by Eq. 2, where higher pO_2 is thermodynamically favorable for the formation of more electrons. In all four cases, as shown in Fig. 6a through Fig. 6a, a decrease in σ_h with an increase in the pH_2O is observed, which is due to the suppression of electron-hole formation, while an increase in σ_H as a function of pH_2O also was observed due to the formation of a thermodynamically stable proton defect as explained in Eq. 1.

Similar trends were observed for other materials. A study carried out by Oishi et al.[51] found a decrease in hole conductivity with an increase in pH_2O for the $BaCe_{0.9}Y_{0.1}O_{3-\delta}$ material. Ji et al.[52] investigated $BaZr_{0.85}Y_{0.15}O_{3-\delta}$ material and obtained conductivity measurements across wide ranges of pO_2 and pH_2O at 800 °C. The experiments demonstrated that at higher pO_2, conductivity decreases with an increase in pH_2O, while it increases at a lower pO_2. The decreasing behavior is mainly attributed to the major contributor of σ_h. Demin et al.[53] found that an increase in pH_2O from 0.003 to 0.32 atm ($pO_2 = 10^{-5}$ atm, T = 600 °C) led to an

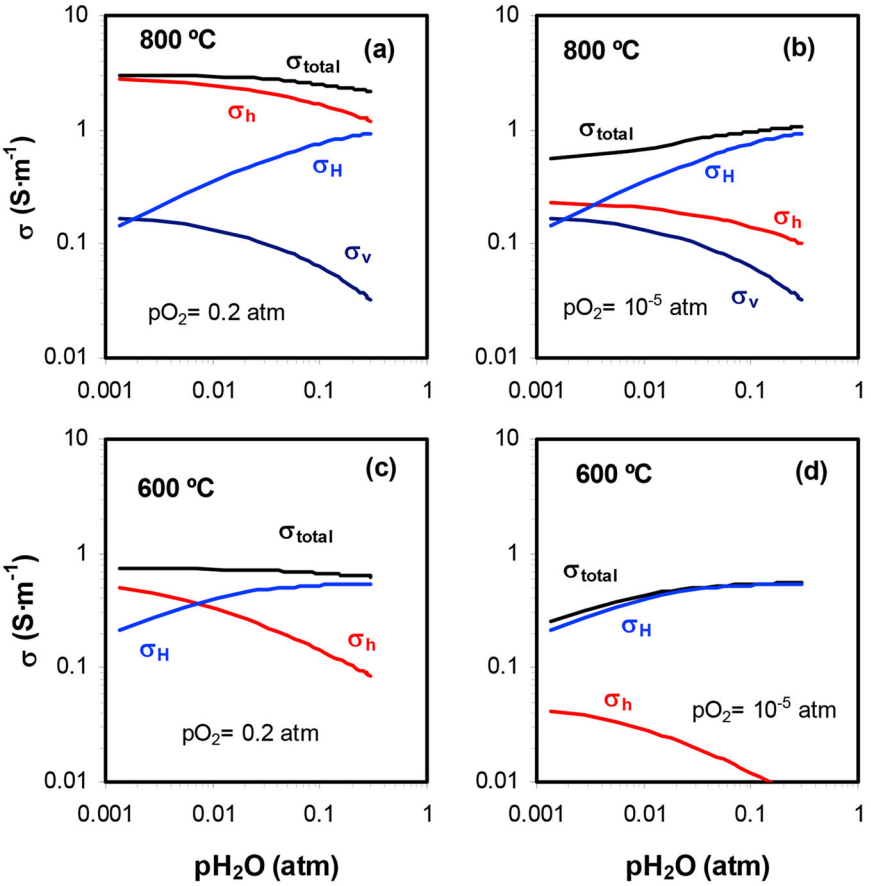

Fig. 6 The representation of partial conductivity of an oxygen-ion, a proton, and an electron hole as a function of partial water pressure at various SOEC operating conditions. a At 800°C and $pO_2 = 0.2$ atm; **b** at 800°C and $pO_2 = 10^{-5}$ atm; **c** at 600°C and $pO_2 = 0.2$ atm; **d** at 600°C and $pO_2 = 10^{-5}$ atm. [Reprinted figure with permission from ref. [49]. Copyright (2017) Elsevier].

increase in the proton transport of $BaZr_{0.8}Y_{0.2}O_{3-\delta}$ material. On a similar material, Han et al.[54] investigated transport properties across a wide range of pO_2 (10^{-25} to 1 atm) with pH_2O varying from 0.03 to 0.51 atm. The authors found that humidification resulted in a gradual increase in the ionic conductivity. In simple terms, increasing pH_2O and decreasing pO_2 helps in increasing the overall faradaic efficiency.

Chemical compositions

Chemical compositions play an important role in the overall conductivity of SOEC materials. In this section, studies related to the effect of A- and B-site doping on the protonic/hole conductivities are included.

Layageva et al.[55] studied the $BaCe_{0.8-x}Zr_xY_{0.2}O_{3-\delta}$ (BCZY) materials. The authors found that increasing the Zr content leads to an increase in hole conductivity, while a decrease in ionic conductivity was observed. At 750°C and a Zr-enriched phase ($x = 0.8$), hole conductivity is predominant. A possible explanation for this behavior is related to: (1) the grain boundary features, where decreasing the grain size results in an increase in both grain boundary density and resistance to ionic transportation, while no detrimental effect on electronic transport is observed; and (2) the grain features, where in case of more packed perovskite structures, the ionic conductivity decreases, while the relative contribution of p-type electronic conductivity increases[32]. Zhang and Zhao[56] studied the transport properties of isovalent substitution of Ba in $BaCeO_3$. The authors investigated the protonic and oxygen conductivity variations in $Ba_{1-x}Sr_xCe_{0.9}Nd_{0.1}O_{3-\delta}$ systems ($x = 0$, 0.1, 0.2). They observed that by decreasing the ionic radius in A cations, with substitution of Sr, results in the structural distortion in the ABO_3 materials, which reduced the oxygen-ion conductivity, while an increase in the proton transport was observed. Kato et al.[57] studied the transport properties of zirconates formed with various alkaline-earth elements (e.g.,$AZr_{0.9}Y_{0.1}O_{3-\delta}$, A = Ca, Sr, Ba, or Ba/Sr). They found that when the A-site is substituted by Ba, the material becomes predominant electronic conduction, as the hole transfer number is equal to 0.72. While, when the A-site is substituted by Sr and Ca, the hole transfer number is equal to 0.33 and 0.15, respectively. These results suggest that a notable difference in the electronic transport variations is observed due to modification in the A-site and B-site of the ABO_3 structures. The conductivity of ABO_3 materials is inversely proportionate to the electro-negativity of the A and B elements[28]. Han et al.[58] investigated the effect of doping elements (e.g., Y, In, Ho, Er, Tm, Yb) on the transport number in $BaZrO_3$. The authors observed that the lowest transport number of electron hole was found for the doping element 'Y.' Furthermore, both Ba-excess and Ba-deficiency led to an increase in the electron hole transport number. The doping element tends to distort the ideal cubic structure to become orthorhombic; further, an increase in the orthorhombic parameter is observed with an increase in the size of the dopant ion. However, Y shows a contrasting trend that yields a smaller parameter, which in turn reduces strain energy and increases defect mobility[59].

External current

Finally, the external current or external applied voltage also have a significant impact on faradaic efficiency. Therefore, many recent

studies have focused on investigating the effect of external current on faradaic efficiencies. Zhu et al.[36] developed a model to predict faradaic efficiency as a function of electrolysis cell operating conditions. They found that faradaic efficiency increases as imposed current density increases. This is because the cell behaves as a concentration cell at an open circuit (e.g., zero imposed current), driving the protons towards the steam side and resulting into reverse proton flux, which leads to a decrease in faradaic efficiency. A similar trend was observed from other studies[60–63]. However, for the same materials and operating conditions, an opposite trend was reported[64–67]. A possible explanation was that as the imposed current density increases, the ohmic heating within the membrane and charge transfer polarization at the electrode–electrolyte interface increase leading to an increase in temperature and a decrease in faradaic efficiency[36]. This discrepancy suggests that there is a knowledge gap, and no published paper explains the discrepancy that can be qualitatively assessed. Thus, more efforts and research are required to study this problem.

Other factors

In addition to the above strategies of lowering the operating temperature, an increase in the partial pressure of H_2O, the doping strategy, and two additional approaches can be used to mitigate electron leakage: (1) the use of an electron-blocking layer between the electrode and the electrolyte, which protects the grains of the electrolyte from reduction and consequently reduces the electronic conductivity;[68,69] and (2) a double-layer electrolyte strategy, especially in the case of Ce-based electrolyte, to block the electron conductivity due to a reduction in Ce[68,70,71].

CURRENT MODELING AND SIMULATION EFFORTS

Computational modeling is a powerful tool that has allowed researchers to physically understand and explain the mechanism behind the experimentally observed properties and trend. Modeling at the atomic/molecular level (e.g., microscale) plays a vital role in understanding the different reaction pathways. It is an effective way to understand or reveal the interaction mechanisms between reactants and the catalytic surface. For this reason, the microscale modeling technique—density functional theory (DFT) – ab initio molecular dynamics (AIMD), molecular dynamics (MD), Monte Carlo (MC), and multiscale modeling approaches are reviewed in detail in the following subsections.

DFT and AIMD modeling

One of the main problems with SOECs is the stability of the materials[72]. DFT has been used in studying the stability and degradation of the materials. Rashkeev et al.[73] developed the DFT and thermodynamic model to investigate the mechanisms of oxygen delamination in SOECs consisting of a YSZ electrolyte and an LSM oxygen electrode. The authors found that the diffusion of atoms across the interface at high temperature significantly affects the structural stability of materials and interfaces. In addition, La and Sr substitutional defects in the ZrO_2 oxide and at the interfaces significantly change the oxygen transport, which may lead to the development of pressure at the interface and eventually leading to the delamination process. Nikolla et al.[74] investigated the stability and degradation of Ni in the presence of carbon-based fuels. They found that alloying the Ni surface increases carbon tolerance by oxidizing the C atoms rather than forming C-C bonds. Similar simulations on Ni and Cu (111) and (211), as well as Cu-Ni and Cu-Co alloys in the presence of CH_4, were carried out by Galea et al.[75]. Despite the fact that C was discovered to have a very high thermodynamic and kinetic barrier to CH_4 dissociation, C was discovered to strongly adsorb onto the Ni (211) surface and grow graphitic carbon over the terrace. This dissociation barrier prevents breakdown and creates possibilities for electrochemical oxidation occurring directly. The Cu-Ni and Cu-Co alloys demonstrated that Ni and Co have little impact on the Cu surface and that the Cu enrichment of the alloy surface limits stability. Raja et al.[76] studied the stability of $BaZrO_3$ at high temperature using AIMD. This study revealed that the high-temperature stability of $BaZrO_3$ is mainly due to the phonon contribution to the free migration energy of the O vacancy. Ribeiro et al.[77] used AIMD-based calculations to study the temperature-dependent phase change in YSZ as a function of Ti content. The results from this study suggest that YSZ structures doped with small amount of Ti are both energetically and kinetically more stable than the undoped YSZ structures, and ideal proportion being 3% TiO_2 for every 1% of Y_2O_3 doping.

DFT-based methods are also used to study hydration, adsorption, dissociation, and diffusion at the interface and in the bulk region. The adsorption, dissociation, and diffusion of hydrogen in pure Ni and the Ni/YSZ slab with two different interfaces (Ni/cation and Ni/O) were studied by Weng et al.[78] using DFT. The H-atom binds preferentially at the hollow site on the Ni surface with an adsorption energy of −2.68 eV, while the H_2 molecule gets adsorbed on the top site of the Ni surface with an adsorption energy of −0.34 eV. The calculated energy barrier for H_2 dissociation on both surface is 0.1 eV. Comparing the diffusion energies of H through the surface and bulk suggests that the surface path is more favorable. In addition, the author found that the barrier for the H migration through Ni/O greater than through Ni/cation. Bhatia et al.[79] used DFT calculations to examine the behavior of hydrogen on three flat Ni surfaces—Ni(100), Ni(110), and Ni(111)—and two stepped Ni surfaces—Ni(531) and Ni(210). It was found that hydrogen diffuses faster on the flat surfaces, but the stepped surface showed a greater mobility in comparison to the diffusion into the metal from the surface layer. Jing et al.[80] performed DFT calculations to investigate the hydration process in yttrium-doped strontium zirconate (SZY) and YSZ materials. The authors found that the SRO(001) surface of SZY and the Ni(111) surface of YSZ is more favorable for water absorption. In the case of proton migrations from surface to bulk, DFT calculations showed that the energy barrier for YSZ is larger than that of SZY for both hydroxide ion migration and proton-hopping. While in the case of proton migration in both bulk structures, the energy barriers are relatively small and comparable. Klarbring et al.[81] used non-equilibrium AIMD to study the diffusion and ionic conductivity in Sm-doped ceria using color diffusion algorithm. In the case of ionic conductivity, the results from AIMD showed good agreement with the experimental values. In case of O–diffusion, the external field used did not influence site preference of the Sm-dopants, which previous studies showed that O-vacancies prefer positions close to Sm atoms[82,83]. AIMD calculations were performed by Fronzi et al.[84] to investigate the proton diffusion in the undoped $BaZrO_3$ cubic structure. Three strain conditions were applied – fully relaxed, isometric tensile strength and compressive strain conditions. The authors found that applied external strain has no-linear effect on the proton diffusion constant and an enhancement in the proton diffusion was observed under compressive strain conditions. Zhu et al.[85] studied the proton diffusion behavior caused by presence of $V_o^{\cdot\cdot}$ in Ca doped BZY_2 material using experimental techniques, DFT and AIMD-based calculations. Experimental study suggested that Ca^{2+} can be successfully doped at the B-site forming the $BZCa_1Y_2$. Due to the weak bond strength of Ca-O bonds, oxygen vacancies tend to form next to Ca, according to DFT simulations. Calculations using AIMD have shown that $BZCa_1Y_2$ has a greater diffusion coefficient than BZY_2, which is supported by the much-decelerated trapping effect with the presence of $V_o^{\cdot\cdot}$.

DFT-based calculations have been used to investigate the role of catalysts on the electrocatalytic activity in electrode-based materials, which affect the electrochemical performance[86]. Using

the DFT model, Cadi-Essadek et al.[87] assessed the stability of various Ni cluster configurations on ZrO_2 and YSZ. The authors found that the formation of an Ni-Ni bond was easier than an Ni-electrolyte interaction. This results in the formation of preferred pyramidal shape instead of flat structures. The stability of Ni clusters was affected by temperature and resulted into the aggregation of Ni-other atoms or clusters. Ingram et al.[88] used DFT calculations and kinetic modeling to investigate relevant reactions associated with the direct utilization of methane on different electrocatalysts. This allowed to compare relative activity of different materials and identify the optimal performing material. The author found that a family of materials (e.g., Ni, Co, Rh, Ru, Ir) offer maximum activity for all relevant reactions. Using DFT-based calculations, Muñoz-García et al.[89] investigated catalytic activity of both Zr substitution with Fe and Mn in a barium zirconate (BZO) environment for oxygen reduction (ORR) and oxygen evolution (OER) reactions. Their study showed that the lowest overpotential as the ORR catalyst was obtained by BZM, while Fe in the stoichiometric BZF surface appears to be insufficient for both ORR and OER. In DFT, the oxygen p-band center has been used for fundamental understanding of an array of perovskite compounds for use in catalyzing the ORR and OER. Properties predictions using the O p-band includes catalytic properties, such as a high-temperature surface exchange rate for the ORR[90,91], binding energies of reaction thermodynamics for ORR and OER[92,93], and overpotentials of ORR and OER in basic solutions[94]. Choi et al.[95] used quantum mechanical calculations (DFT and AIMD) to study the ORR on Sr-doped $LaMnO_3$. The authors found that B cations are more active than A cations for oxygen reduction on a number of perovskite-type ABO_3 cathodes is supported by the fact that O_2 species are preferentially adsorbed on the Mn site rather than the La site. A DFT-based study carried out by Jacobs et al. [96] suggests that under a consistent computational framework, robust linear correlations between a variety of significant metrics of catalytic activity and the oxygen p-band bulk descriptor can be found. More DFT-based studies on different aspects of electrode materials can be found elsewhere[97].

DFT calculations have been used in investigating defect chemistries and thermodynamics, which gives insights about SOEC materials in operating conditions. Bjørheim et al.[98] for the first time, used first-principle calculations to investigate the phonon contribution to the defect thermodynamics ($V_o^{\cdot\cdot}$ and $OH_o^{\cdot}$) of the ZrO_2 terminated (001) surface of $BaZrO_3$ material. The vibrational formation entropy of the surface $V_o^{\cdot\cdot}$ is significantly higher than that of the bulk $V_o^{\cdot\cdot}$, which is due to the smaller structural relaxations. However, in case of the $OH_o^{\cdot}$, it displays near identical vibrational spectra at the surface and in the bulk structure. Using first-principle DFT calculations, Bjørheim et al.[99] investigated the impact of phonons on the hydration and defect thermodynamics of undoped and acceptor (e.g., Sc, In, Y, Gd) doped $BaZrO_3$ material. They found that for all of the dopants, the vibrational formation entropy of oxygen vacancy is significantly lower than the protonic defect, which is also the dominant contributor to the entropy of hydration. In addition, the calculated hydration entropy becomes more negative in the order of Y < Gd < In < Sc, because both the formation energy and vibrational formation entropy of oxygen vacancy and protonic defect become more negative with increasing dopant ion size. In addition, Bjørheim et al.[100] also investigated the structural, electronic and thermodynamic properties of neutral and positively doubly charged oxygen vacancies in $BaZrO_3$ using AIMD calculations. The author observed that, due to both the charged oxygen vacancy's severe deformation of the local structure and its substantial negative formation volume, phonons are demonstrated to contribute significantly to the charged oxygen vacancy's formation energy at high temperatures (1 eV at 1000 K). The ensuing lattice distortions for the neutral vacancy, and consequently the phonon contributions to the free formation energy, are much less. As a result, from 0 K to 1000 K, the charge transition level for oxygen vacancies (+2/0) varies from 0.42 to 0.83 eV below the conduction band bottom due to phonon effects on the relative stability of the two defects. By combining the ab initio results with thermodynamics modeling, defect formation at finite temperature and pressure were investigated by Björketun et al.[101], who found that protonic defects are thermodynamically stable only at low temperatures, which is in agreement with the empirical results. By taking into account the configuration of complex defects, Takahashi et al.[102] investigated the influence of fundamental factors that affect the hydration of $BaZrO_3$ doped with trivalent cations (e.g., Al, Sc, Ga, Y, In, Lu). They found that Al- and Ga-doped BZOs are more likely to form oxygen vacancies, which results in low hydration energies and stable proton sites at the closest neighbor (1NN). However, $BaZrO_3$ that have been doped with Y, In, and Lu prefer protons at the second nearest neighbor (2NN). DFT-based thermodynamic modeling was performed by Lee et al.[103] to investigate the effect of humidity and pressure of H_2/O_2 gas on the defect chemistry and transport characteristics of BZY in the temperature range of 800 to 1200 K. The authors found that oxygen vacancies formed to compensate for extra Ba vacancies may cause a slight increase in protonation, while a decrease in overall proton diffusivity was observed due to trapping of protons near the Ba vacancies. DFT and AIMD-based calculations have also been used to study the generation, migration, dissociation and transport of electron-hole pairs in photovoltaic or solar cells[104,105]. Similar studies can also be performed to study the electron-hole pair migration and interactions in the SOECs.

Screening new materials and performing fundamental research can be easily enabled through the Material Genome Initiative (MGI)[106,107] database, and DFT and AIMD-based studies have been successfully using the MGI database in exploring new materials[108,109]. MGI is of significant importance to expedite the material discovery and development process.

The main issue with DFT and AIMD-based studies is the limit on the number of atoms that can be efficiently simulated. In addition, temperature-dependent phenomena and harsh environmental chemistries (e.g., electron migration energy calculations, secondary chemistry calculations with explicit electrons in the system) that tend to lower the faradaic efficiency cannot be simulated using DFT. Also, the timescale that DFT simulations could access is another limiting factor.

MD modeling

In recent years, MD studies have played a crucial role in studying the effect of grain boundaries (GBs) on the oxygen diffusion pathway and proton diffusion in different SOEC materials, especially electrolyte materials. Chang et al.[110] studied the GB effect of ionic transport at higher temperatures using Buckingham potential in MD. This study also showed the presence of GBs, degraded ion transport characteristics. At lower temperatures, GBs dominate ion transport, while at higher temperatures, the influence of GBs was eliminated because the migration energy barrier was overcome. Fisher et al.[111] studied the oxygen diffusivity in pure zirconia and 8 mol% YSZ over a temperature range of 1273 to 2673 K using MD. The authors found that open GB enables oxygen transport and the rate of diffusion in the bulk structure of YSZ crystals is slow. A number of intrinsic vacancies are present at the interface of pure ZO_2 bicrystals, according to MD simulations, and these promote GB diffusion at elevated temperatures[112]. An MD study by Fisher et al.[113] investigated the structure and ion transport properties of three interfaces in 8 mol% YSZ, which included tilt and twist GBs. The authors found that symmetrical tilt GB decreases the overall conductivity because of the trapping of vacancies in the GB region. However, twist GB enables rapid diffusion with an opportunity to provide means for enhancing the

ionic conductivity of YSZ ceramics. Gonzalez-Romero et al.[114] studied the physical characteristics (e.g., GB energies and oxygen diffusion) of Σ3, Σ5, Σ11, and Σ13 GBs in model of YSZ bicrystals as a function of the concentration of yttria and temperature. Lee et al.[115] performed a hybrid MC-MD modeling study on the defect distribution near tilt GBs in YSZ and gadolinia-doped ceria (GDC) materials. They found that in both materials, oxygen vacancy segregation precedes dopant segregation near the GB. Moreover, GDC showed a stronger dopant segregation than YSZ despite a smaller size mismatch between host and dopant cations. From this result, the authors made a conclusion that dopant segregation is initiated by vacancy segregation and largely controlled by dopant-vacancy association. Similarly, many MD studies on the GBs of YSZ material have been studied[116–119].

MD studies have successfully been used to describe how the concentration of doping elements can affect oxygen migration, oxygen diffusivity, and defect interactions. Using Buckingham-type potentials in MD, Devanathan et al.[120] studied the effect of doping concentration on oxygen migration and defect interactions in YSZ. They found that with 6 to 25 mol% yttria in YSZ, the activation energy of oxygen diffusion was found to be 0.6 to 1.0 eV. Also, the formation of $Y-V_o^{\cdot\cdot}-Y$ with a binding energy of −0.85 eV could play an important role in any conductivity degradation of YSZ. Oxygen vacancy migration properties were studied by Kilo et al.[121] by using experimental and MD methods (Buckingham potential). The authors found that experimentally, the oxygen diffusion was highest for the 10 mol% yttria in YSZ. While MD results consistently showed higher diffusion coefficient values than the experiments, the MD predicted activation enthalpy of migration showed a good agreement with the experimental results. Araki et al.[122] studied the oxygen diffusion in 4, 8, and 14 mol% yttria (e.g., 4YSZ, 8YSZ, 14YSZ) in YSZ subjected to uniaxial tension in the [100], [110], and [111]. An increase in the oxygen diffusivity along the tensile direction in all three cases (e.g., [100], [110], [111]) was observed for 4YSZ and 8YSZ. However, in the case of 14YSZ, the oxygen diffusivity remained unchanged, probably due to the higher yttria content. Shimojo et al.[123] investigated the structural and dynamical properties of YSZ for the three dopant concentration—4.85, 10.2, and 22.7 mol% yttria in YSZ. The authors found that dopant Y ions play a significant role in oxygen diffusion. At lower dopant concentration, Y ions promote the migration of O ions; however, as the concentration increases, a decrease in diffusion constant was observed. The restriction by the Y-Y edge causes a decrease in the diffusivity with an increase in the dopant concentration[124].

In addition, phase composition and structural stability were analyzed using MD. Ogawa et al.[125] modeled zirconia polycrystal and investigated the microscopic mechanism of high-temperature deformation. The material was deformed at 1500 K under tensile stress up to 8 GPa. The model was found to be stable up to 2 GPa, and largely elongated at stresses above 6 GPa. A disordered layer at the GB was observed and seemed to play an important role in the deformation process. Chang et al.[126] investigated the effect of the cubic/monoclinic phase composition on the oxygen-ion diffusion in zirconia-based solid electrolytes using Born-Meyer-Buckingham potential in MD. They found that due to the presence of an unfavorable monoclinic structure for small-ion penetration, the pure cubic-phase system had more effective thermal motions with extended and continuous movements than the dual-phase system. The diffusion coefficient analysis revealed that the pure monoclinic structure was unaffected by the material composition, while the phase and material composition controlled the diffusion mechanisms.

Most of the above MD studies used short-range Buckingham potential and long-range Coulombic potential for investigating different aspects in the SOEC materials. The Buckingham potential is a simplified version of the Lennard-Jones potential, which cannot accurately capture the effects of temperature and pressure on the interaction between atoms. On the other hand, the reactive potential - ReaxFF developed by van Duin et al.[127] includes many-body interactions, which allows for accurate interactions between the atoms. ReaxFF also considers the effect of temperature and pressure on the interactions between atoms, which is of significant importance in case of accurate predictions of SOEC materials in different conditions.

In 2008, van Duin et al.[128] developed a ReaxFF to study proton diffusion across the GB using the MD simulations. This study paved the way for decades-long simulations using ReaxFF. Cammarata et al.[129] studied the structural changes and proton mobility for the undoped, singly, and doubly Y-doped $BaZrO_3$ with varying temperatures ranging from 100–1200 K using ReaxFF MD. The MD results well-reproduced the behavior already observed by the quantum mechanics (QM) calculations where two important conclusions were inferred: (1) the clustering of yttrium in BZY were seen; and (2) out of the three oxygen site sets, two yttrium-clustered models acted as multilevel protonic traps, which delayed the protonic diffusion in the bulk. This was due to the large number of proton-hopping events that occurred between those oxygen atoms that were surrounded by clustered yttrium atoms. Thus, proton conductivity in these materials can be improved by avoiding such clustering. Li et al.[130] studied the O^{2-} transport properties, as well as the migration mechanism in Y doped $BaZrO_3$ with/without edge dislocations using ReaxFF MD. In addition, they studied the effect of dopant concentration and temperature on thermodynamic and kinetic properties of bulk and dislocation system. The authors found that below 20 mol% Y content in BZY, O^{2-} ion conduction is promoted, while the maximum O^{2-} conductivity was observed for the model having 30 mol% Y doped in dislocated BZY. Moreover, dislocations in the model accelerate the O^{2-} diffusion when the temperature is less than 1173.15 K due to the formation of double-bottle diffusion channels. Using ReaxFF MD, Ottochian et al.[131] studied the effect of isotropic and biaxial strain on proton conduction in Y-doped $BaZrO_3$ at different temperatures (e.g., 1500–2000 K). They observed that compressive pressure led to an increase in the proton conductivity, while the effect of biaxial strain is more complex. In the case of intermediate biaxial strain, an increase in the proton conductivity was observed because of the shortened O-O distance. However, an opposite trend was observed in case of higher compressive biaxial strain, due to strong localization of proton far from the B-site cations. Merinov et al.[132] developed a ReaxFF force field for studying the electrode–electrolyte interface. These parameters have facilitated to re-calculate the primary energy barrier for proton diffusion in BZY which shows a good agreement with experimental values. More MD-based studies with different FF can be found elsewhere[133].

The inaccuracy in predicting the electron affinity or ionization potential restricts the applicability of ReaxFF in redox reactions[134]. This led to the development of an electron version of ReaxFF termed 'eReaxFF.'[135] In this potential, electrons-like or hole-like particles are explicitly included. This method has been successfully used to simulate the electronic motion in carbon-based[135], lithium-electrolyte[136], Ag metal[137], and polyethylene electrical breakdown systems[138].

As mentioned previously, electron holes (e.g., electronic conductivity) significantly decrease faradaic efficiency. Therefore, to simulate electronic current leakage, the electrons/hole pair should be explicitly included, which is currently not involved in almost all force fields, except for the eReaxFF. However, the parallel version is only incorporated in the Amsterdam Density Functional package[139]. Since the parallel version is still not available in most MD software packages, the dependency of the serial version is increased, which ultimately limits the size of the eReaxFF MD that can be efficiently simulated.

In addition to the classical interatomic force fields, recently, machine-learned force fields (MLFF) have emerged as an ideal

solution to drastically augment length and timescales accessible to MD simulations and retaining first-principle accuracy. Verdi et al.[140] developed a MLFF based on MD and Bayesian interface to describe the thermodynamic properties of zirconia. This MLFF accurately captured the temperature-induced phase transformation below the melting point. Guan et al.[141] recently developed a global neural network potential (G-NN) for the YSZ. They carried long-time molecular dynamics simulations for YSZ at 6.7, 8, 10, and 14.3 mol % over a wide temperature range (800–2000 K). In addition, Guan et al.[142] developed a stochastic surface walking global exploration with G-NN potential (SSW-NN) to investigate changes in the microstructure of YSZ with different concentrations of Y. Wang et al.[143] developed a MLFF to investigate anisotropic fracture behavior of $BaZrO_3$ material. The author observed that the fracture strength in the [110] crystal orientation is more significant than the [100] crystal orientation. Niu et al.[144] using AIMD and machine learning molecular dynamics (MLMD) studied the proton migration in Y-doped $BaZrO_3$ material. The author observed that at shorter time, the performs superdiffusion through the O–H, while at longer time, proton diffusion first becomes subdiffusive due to OH ion rotation and then gradually turns to normal diffusion. Kholtobina et al.[145] investigated the temperature dependencies of surface energies for (111) and (110) CeO_2 with extended two-stage up-sampled thermodynamic integration using Langevin dynamics (TU-TILD). This method was used together with machine learning potentials called moment tensor potentials (MTP). The authors found that the increase in the temperature from 0 to 2100 K led to the decrease of the Helmholtz free energy of (111) CeO_2 from 0.78 to 0.64 Jm^{-2}.

MC modeling

This section includes a review of MC-based studies on the order of reaction mechanism, oxygen diffusivity, conductivity, electrode degradation, and defect interactions. Some important processes and aspects of cell physics occur on a timescale much longer than the MD timescale (e.g., in nanoseconds). MC methods, which are at a larger length and timescales are suited to study these phenomena. MC-based modeling does not include identifying new reaction pathways, but rather focuses on the complexities associated with the interaction of particles[146]. Modak and Lusk[146] used kinetic MC (KMC) techniques to simulate open circuit voltage and an electrical double layer of doped electrolyte. The study was mainly focused on electrical-physical processes and the results from KMC modeling showed a good agreement with the predictions from the analytical model. The main idea for developing these algorithms was to use it as a sub-model in a more complex and realistic KMC simulator, which accounts for oxidation reaction on the surface of the anode.

KMC has also been used to investigate the reaction mechanism and oxygen-ion diffusion conductivity. Pornprasertsuk et al.[147] performed KMC simulations based on DFT-calculated barrier energies to determine the dopant concentrations dependency on the oxygen self-diffusion coefficient in $(Y_2O_3)_x$ $(ZrO_2)_{(1-2x)}$ with x varying from 6 to 15%. DFT results suggest that a decrease in the conductivity with a higher dopant concentration is due to the higher migration energy required to travel across two adjacent Y-Zr and Y-Y pairs. While the KMC results reveal that the increase in migration energy is due to the higher probability of oxygen vacancies encountering Y-Zr and Y-Y pairs. Another study by Pornprasertsuk et al.[148] used quantum calculation-based KMC to study oxide-ion diffusion process and the space charge double layer at the electrode–electrolyte interface subject to applied alternating potentials, as well as the dependence of impedance and double layer capacitance on the thickness of the electrolyte. The simulation showed that at lower frequencies, oxide ions have sufficient time to migrate across the electrolyte and accumulate at the electrode–electrolyte interface creating a double layer with a space charge. Longer time is needed for thicker electrolytes to reach the same level of oxide-ion vacancies at the electrode–electrolyte interface. Wang et al.[149] developed a KMC model based on a series of reversible elementary steps for simulating ORR at the cathode-electrolyte interface and hydrogen-oxidation mechanism near the anode-electrolyte interface. They found that increasing applied bias voltage, operating temperature, and relative permittivity YSZ and decreasing the thickness of YSZ increased the ionic current density and efficiency of the cell. Krishnamurthy et al.[150] developed a DFT-based KMC model to study the diffusion of oxygen in YSZ. Oxygen diffusivity was found to increase with an increase in the yttria mole fraction before attaining a maximum value of ~0.1 mole fraction yttria. To understand the physical mechanisms underlying the observed behavior, analytical models were developed. Based on the analyses, two factors that explained the observed behavior were: (1) an increase in the number of high migration energy Y-Zr and Y-Y edges; and (2) an increased dopant induced and vacancy dopant correlations at higher yttria content. Dholabhai et al.[151] used a DFT-based kinetic lattice Monte Carlo (KLMC) model to investigate the optimal dopant concentration in GDC for maximum ionic conductivity. They found that higher dopant concentrations increase the vacancy concentration, which thus increases ionic conductivity. However, at higher concentrations, vacancy-vacancy repulsion impedes the diffusion process, which thus reduces the ionic conductivity. At a 20 to 25% mole fraction of Gd, the maximum ionic conductivity was predicted. Gunn et al.[152] developed hybrid MC (HMC) and adaptive KMC (AKMC) models based on Buckingham potentials to study the thermodynamic equilibrium and kinetic properties in the gadolinium-doped ceria (GDC). HMC demonstrated the movement of oxygen vacancy from bulk to surface, while the AKMC was crucial in finding multi-atom concerted diffusion mechanisms spanning over large distances.

Other factors like the aging of electrodes and defect interactions were also studied using MC. The KMC simulation model developed by Zhang et al.[153] was used to study the thermal aging of infiltrated electrodes by considering the surface diffusion mechanism. The effects of temperature, infiltration loading, wettability, and electrode configuration were studied, as well as the geometric parameters, which included the infiltrate particle size, the total and percolated quantities of the three-phase boundary length and infiltrate surface area, and the tortuosity factor of the infiltrate network. This parametric study led to the following conclusions: (1) lowering the temperature can slow the degradation kinetics of triple-phase boundaries (TPB) and the surface area of the infiltrate particle; however, it can lead to a high level of tortuosity factor of the infiltrate network and slow the electrode reaction kinetics; (2) increasing the infiltration loading accelerates the coarsening rate of infiltrate particles; (3) increasing the wettability increases the coarsening rate of the infiltrate particles and decreasing rate of TPB; and (4) the tortuosity factor of the infiltrate network decreases with time and eventually attains stability. Eisele et al.[154] developed a DFT-based Metropolis MC (MMC) model to estimate the influence of defect interactions on the hydration of BZY. The results that were obtained concluded that the non-ideal experimental behavior for the varying yttrium fraction, proton fraction, and temperature were due to the ionic defect interactions. The DFT-based KMC model developed by Gomez et al.[155] showed that the proton conduction can be hampered by the presence of other protons. Using the thermogravimetric and a.c. impedance study, similar behavior was observed by Yamazaki et al.[156].

KMC models usually use physical property data generated by DFT, MD, or experimental analyses. If inaccurate parameters are selected at the DFT level, then the output from the KMC studies will yield inaccurate results. In the case of a large number of

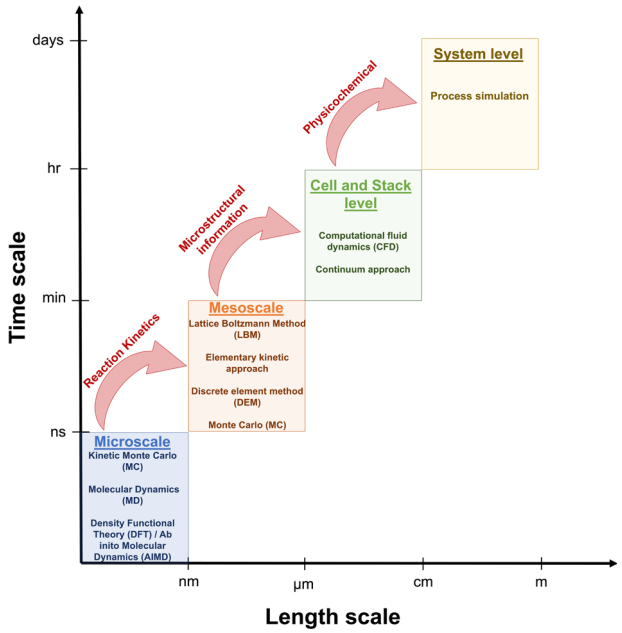

Fig. 7 Schematic diagram of exchange of information between different length-scale models.

variables confined to different constraints, KMC can be computationally inefficient.

Multiscale modeling

The operation of a cell depends on complex interactions between multi-physics, such as multi-phase fluid flow, mass transport, heat transfer, and electrochemical reactions. Multiscale modeling provides an opportunity to give a mechanistic description of material performance, and thus to guide optimization designs of material and structure. Therefore, handshaking of different length-scale studies, as observed in Fig. 7, will improve the understanding of SOEC properties and their effects on the SOEC behavior.

Ma et al.[157] developed a multiscale model combining DFT, transition state theory (TST), and continuum modeling for the oxygen-based reactions at the electrode to elucidate critical steps and predict device performance. The reaction rates predicted from TST were used as an input in the continuum model for obtaining overpotential-current density relations. The proposed multiscale model yields a quantitative agreement with the overpotential-current density data from the experiments. A new hybrid molecular-continuum model-pointwise coupling methodology was presented by Asproulis et al.[158]. The atomistic models were utilized to calculate transport properties, provide accurate boundary conditions, and substitute constitutive relations for the pressure among others, while the solution was advanced through the continuum solver. The calculation of the macroscopic variables was performed through averaging the corresponding microscopic properties. Ren et al.[159] investigated the effect of oxygen vacancy location on CO_2 reduction reaction at the three-phase boundary of Ni/samarium-doped ceria surface using DFT calculations. Moreover, based on the DFT results, the microkinetic model was developed to determine the rate-controlling step under different operating voltages at 1000 K. The results reveal that in case of interface oxygen vacancy, CO desorption is the rate-controlling step regardless of electrode overpotentials. However, in the case of non-interface oxygen vacancy, the rate-controlling step will change with an increase in cathode overpotential.

A multiscale approach was developed by Khaleel et al.[160], in which the microscale electrochemistry model (e.g., Lattice-Boltzmann algorithm) calculates the performance of the porous electrode material based on the distribution of reaction surfaces, the material structure at the microstructure level, and the oxygen-ion transport through the material. The macroscale calculations (MARC software) were used to calculate the current density, cell voltage, and heat production after the microscale electrochemistry modeling has calculated the total fuel cell current-voltage relation. Studies by Cheng et al.[161] and Pasaogullari and Wang et al.[162] also showed the usage of the multiscale modeling approach; however, the integration of different scales is not mentioned. Other multiscale modeling approaches and modeling studies at a higher length-scale (e.g., cell and stack level, system level) can be found elsewhere[163,164].

The development of methods for multiscale multi-physics modeling that consider the coupling of fluid flow, heat transfer, species transport, and electrochemical kinetics is a challenge for future studies as this multiscale modeling coupling is rare[165–167].

FUTURE PERSPECTIVES AND PATH FORWARD

Despite the advantageous capabilities of SOECs for green H_2 production, its use is still limited on the industrial scale. The selections of materials for the cathode, anode, and electrolyte all play a crucial role in the performance of a cell. At the individual level, each component of the cell needs to be 100% effective and efficient to utilize the promising features of SOECs.

The main issue with electrolyte materials is current leakage due to a non-negligible electron conduction, which decreases faradaic efficiency. A computational model is a powerful tool that can be used to systematically study, analyze, and understand the problems related to current leakage within electrolytes. On the atomistic level, DFT studies can be performed to understand the surface chemistries and electron-hole mobility, which is directly related to current leakage. On the other hand, MD studies can be used to investigate the effect that temperature has on electron/hole formation, as well as mobility and bulk chemistries, by using methods that explicitly include electron/hole pair modeling such as AIMD and eReaxFF. Explicit electron/hole pair modeling also can be useful in understanding the factors affecting the faradaic efficiency of the cell and H_2 generation. In addition, MC simulations in combination with DFT/MD can be used to investigate the defect evolution and accumulation on a larger timescale. Finally, the multiscale modeling approach plays a significant role in understanding complex processes at a different length scale. The handshaking of a different length-scale study will help in solving the current problems like faradaic efficiency related to SOECs.

In addition to a different length-scale study, the implementation of parallel methods like the graphics processing unit in a different length-scale software package such as MD will help computational modelers in the future to simulate larger models. Incorporating the MGI database with machine learning techniques and data analysis will expedite the process of investigating and exploring new materials related to SOECs, which will significantly help the scientific community.

DATA AVAILABILITY

Data sharing is not applicable to this article as no datasets were generated or analyzed during the current study.

CODE AVAILABILITY

No underlying code was developed for this study.

Received: 31 October 2022; Accepted: 12 May 2023;
Published online: 21 August 2023

REFERENCES

1. Zhou, Y. et al. Green hydrogen: a promising way to the carbon-free society. *Chin. J. Chem. Eng.* **43**, 2–13 (2022).
2. Mohanty, R., Mansingh, S., Parida, K. & Parida, K. Boosting sluggish photocatalytic hydrogen evolution through piezo-stimulated polarization: a critical review. *Mater. Horiz.* **9**, 1332–1355 (2022).
3. Gao, F.-Y., Yu, P.-C. & Gao, M.-R. Seawater electrolysis technologies for green hydrogen production: challenges and opportunities. *Curr. Opin. Chem. Eng.* **36**, 100827 (2022).
4. Kuang, M. et al. Interface engineering in transition metal carbides for electrocatalytic hydrogen generation and nitrogen fixation. *Mater. Horiz.* **7**, 32–53 (2020).
5. Ball, M. & Weeda, M. The hydrogen economy–vision or reality? *Int. J. Hydrog. Energy* **40**, 7903–7919 (2015).
6. Nicodemus, J. H. Technological learning and the future of solar H2: a component learning comparison of solar thermochemical cycles and electrolysis with solar PV. *Energy Policy* **120**, 100–109 (2018).
7. Yadav, D. & Banerjee, R. Economic assessment of hydrogen production from solar driven high-temperature steam electrolysis process. *J. Clean. Prod.* **183**, 1131–1155 (2018).
8. Bhandari, R., Trudewind, C. A. & Zapp, P. Life cycle assessment of hydrogen production via electrolysis–a review. *J. Clean. Prod.* **85**, 151–163 (2014).
9. Xiang, C., Papadantonakis, K. M. & Lewis, N. S. Principles and implementations of electrolysis systems for water splitting. *Mater. Horiz.* **3**, 169–173 (2016).
10. Mehmeti, A., Angelis-Dimakis, A., Muñoz, C. B., Graziadio, M. & McPhail, S. J. Ecothermodynamics of hydrogen production by high-temperature electrolysis using solid oxide cells. *J. Clean. Prod.* **199**, 723–736 (2018).
11. Nicita, A., Maggio, G., Andaloro, A. P. F. & Squadrito, G. Green hydrogen as feedstock: financial analysis of a photovoltaic-powered electrolysis plant. *Int. J. Hydrog. Energy* **45**, 11395–11408 (2020).
12. Yu, M., Wang, K. & Vredenburg, H. Insights into low-carbon hydrogen production methods: green, blue and aqua hydrogen. *Int. J. Hydrog. Energy* **46**, 21261–21273 (2021).
13. Pandiyan, A., Uthayakumar, A., Subrayan, R., Cha, S. W. & Krishna Moorthy, S. B. Fabrication and performance of micro-tubular solid oxide cells. *Energies* **8**, 2–22 (2019).
14. Bi, L., Boulfrad, S. & Traversa, E. Steam electrolysis by solid oxide electrolysis cells (SOECs) with proton-conducting oxides. *Chem. Soc. Rev.* **43**, 8255–8270 (2014).
15. Malavasi, L., Fisher, C. A. J. & Islam, M. S. Oxide-ion and proton conducting electrolyte materials for clean energy applications: structural and mechanistic features. *Chem. Soc. Rev.* **39**, 4370–4387 (2010).
16. Brett, D. J. L., Atkinson, A., Brandon, N. P. & Skinner, S. J. Intermediate temperature solid oxide fuel cells. *Chem. Soc. Rev.* **37**, 1568–1578 (2008).
17. Shi, H., Su, C., Ran, R., Cao, J. & Shao, Z. Electrolyte materials for intermediate-temperature solid oxide fuel cells. *Prog. Nat. Sci.* **30**, 764–774 (2020).
18. Ye, L. & Xie, K. High-temperature electrocatalysis and key materials in solid oxide electrolysis cells. *J. Energy Chem.* **54**, 736–745 (2021).
19. Liu, L. et al. Composite ceramic cathode La0. 9Ca0. 1Fe0. 9Nb0. 1O3-δ/Sc0. 2Zr0. 8O2− δ towards efficient carbon dioxide electrolysis in zirconia-based high temperature electrolyser. *Int. J. Hydrog. Energy* **42**, 14905–14915 (2017).
20. Wang, Y., Li, W., Ma, L., Li, W. & Liu, X. Degradation of solid oxide electrolysis cells: phenomena, mechanisms, and emerging mitigation strategies—a review. *J. Mater. Sci. Technol.* **55**, 35–55 (2020).
21. Fabbri, E., Pergolesi, D. & Traversa, E. Materials challenges toward proton-conducting oxide fuel cells: a critical review. *Chem. Soc. Rev.* **39**, 4355–4369 (2010).
22. Jing, J. et al. Structure, synthesis, properties and solid oxide electrolysis cells application of Ba (Ce, Zr) O3 based proton conducting materials. *Chem. Eng. J.* **429**, 132314 (2022).
23. Katahira, K., Kohchi, Y., Shimura, T. & Iwahara, H. Protonic conduction in Zr-substituted BaCeO3. *Solid State Ion.* **138**, 91–98 (2000).
24. Ma, G., Shimura, T. & Iwahara, H. Ionic conduction and nonstoichiometry in BaxCe0. 90Y0. 10O3− α. *Solid State Ion.* **110**, 103–110 (1998).
25. Shima, D. & Haile, S. M. The influence of cation non-stoichiometry on the properties of undoped and gadolinia-doped barium cerate. *Solid State Ion.* **97**, 443–455 (1997).
26. Matsuzaki, Y. et al. Modified energy efficiencies of proton-conducting SOFCs with partial conductions of oxide-ions and holes. *Fuel Cells* **19**, 503–511 (2019).
27. Matsuzaki, Y. et al. Relationship between electrochemical properties and electrolyte partial conductivities of proton-conducting ceramic fuel cells. *ECS Trans.* **78**, 441 (2017).
28. Zhang, W. & Hu, Y. H. Progress in proton-conducting oxides as electrolytes for low-temperature solid oxide fuel cells: From materials to devices. *Energy Sci.* **9**, 984–1011 (2021).
29. Matsuzaki, Y. et al. Suppression of leakage current in proton-conducting BaZr0. 8Y0. 2O3− δ electrolyte by forming hole-blocking layer. *J. Electrochem. Soc.* **167**, 084515 (2020).
30. Lei, L. et al. Progress report on proton conducting solid oxide electrolysis cells. *Adv. Funct. Mater.* **29**, 1903805 (2019).
31. Duncan, K. L., Lee, K.-T. & Wachsman, E. D. Dependence of open-circuit potential and power density on electrolyte thickness in solid oxide fuel cells with mixed conducting electrolytes. *J. Power Sources* **196**, 2445–2451 (2011).
32. Zvonareva, I., Fu, X.-Z., Medvedev, D. & Shao, Z. Electrochemistry and energy conversion features of protonic ceramic cells with mixed ionic-electronic electrolytes. *Energy Environ. Sci.* **15**, 439–465 (2022).
33. Iwahara, H., Esaka, T., Uchida, H. & Maeda, N. Proton conduction in sintered oxides and its application to steam electrolysis for hydrogen production. *Solid State Ion.* **3**, 359–363 (1981).
34. Babiniec, S. M., Ricote, S. & Sullivan, N. P. Characterization of ionic transport through BaCe0. 2 Zr0. 7Y0. 1O3− δ membranes in galvanic and electrolytic operation. *Int. J. Hydrog. Energy* **40**, 9278–9286 (2015).
35. Lei, L., Tao, Z., Wang, X., Lemmon, J. P. & Chen, F. Intermediate-temperature solid oxide electrolysis cells with thin proton-conducting electrolyte and a robust air electrode. *J. Mater. Chem. A.* **5**, 22945–22951 (2017).
36. Zhu, H., Ricote, S. & Kee, R. J. Faradaic efficiency in protonic-ceramic electrolysis cells. *J. Phys. Energy* **4**, 014002 (2022).
37. Loureiro, F. J. A. et al. Proton conductivity in yttrium-doped barium cerate under nominally dry reducing conditions for application in chemical synthesis. *J. Mater. Chem. A.* **7**, 18135–18142 (2019).
38. Zvonareva, I. A. et al. Heavily Sn-doped barium cerates BaCe0. 8–xSnxYb0. 2O3–δ: correlations between composition and ionic transport. *Ceram. Int.* **47**, 26391–26399 (2021).
39. Grimaud, A. et al. Transport properties and in-situ Raman spectroscopy study of BaCe0. 9Y0. 1O3− δ as a function of water partial pressures. *Solid State Ion.* **191**, 24–31 (2011).
40. Kuroha, T. et al. Optimum dopant of barium zirconate electrolyte for manufacturing of protonic ceramic fuel cells. *J. Power Sources* **506**, 230134 (2021).
41. Hyodo, J. et al. Determination of oxide ion conductivity in Ba-doped LaYbO3 proton-conducting perovskites via an oxygen isotope exchange method. *J. Phys. Chem. C.* **125**, 1703–1713 (2021).
42. Yu, S. et al. Enhancing the sinterability and electrical properties of BaZr0. 1Ce0. 7Y0. 2O3-δ proton-conducting ceramic electrolyte. *J. Am. Ceram. Soc.* **104**, 329–342 (2021).
43. Rasaki, S. A., Liu, C., Lao, C. & Chen, Z. A review of current performance of rare earth metal-doped barium zirconate perovskite: The promising electrode and electrolyte material for the protonic ceramic fuel cells. *Prog. Solid State Chem.* **63**, 100325 (2021).
44. Hwang, S. H., Kim, S. K., Nam, J.-T. & Park, J.-S. Fabrication of an electrolyte-supported protonic ceramic fuel cell with nano-sized powders of Ni-composite anode. *Int. J. Hydrog. Energy* **46**, 1076–1084 (2021).
45. Bae, K., Kim, D. H., Choi, H. J., Son, J. W. & Shim, J. H. High-performance protonic ceramic fuel cells with 1 μm Thick Y: Ba (Ce, Zr) O3 electrolytes. *Adv. Energy Mater.* **8**, 1801315 (2018).
46. Tarutin, A. P. et al. Performance of Pr2 (Ni, Cu) O4+ δ electrodes in protonic ceramic electrochemical cells with unseparated and separated gas spaces. *J. Mater. Sci. Technol.* **93**, 157–168 (2021).
47. Liang, M. et al. Nickel-doped BaCo0. 4Fe0. 4Zr0. 1Y0. 1O3-δ as a new high-performance cathode for both oxygen-ion and proton conducting fuel cells. *Chem. Eng. J.* **420**, 127717 (2021).
48. Kim, D., Son, S. J., Kim, M., Park, H. J. & Joo, J. H. PrBaFe2O5+ δ promising electrode for redox-stable symmetrical proton-conducting solid oxide fuel cells. *J. Eur. Ceram. Soc.* **41**, 5939–5946 (2021).
49. Heras-Juaristi, G., Pérez-Coll, D. & Mather, G. C. Temperature dependence of partial conductivities of the BaZr0. 7Ce0. 2Y0. 1O3-δ proton conductor. *J. Power Sources* **364**, 52–60 (2017).
50. Merkle, R., Hoedl, M. F., Raimondi, G., Zohourian, R. & Maier, J. Oxides with mixed protonic and electronic conductivity. *Annu. Rev. Mater. Res.* **51**, 461–493 (2021).
51. Oishi, M. et al. Defect structure analysis of B-site doped perovskite-type proton conducting oxide BaCeO3: Part 2: The electrical conductivity and diffusion coefficient of BaCe0. 9Y0. 1O3− δ. *Solid State Ion.* **179**, 2240–2247 (2008).
52. Ji, H.-I. et al. Three dimensional representations of partial ionic and electronic conductivity based on defect structure analysis of BaZr0. 85Y0. 15O3− δ. *Solid State Ion.* **203**, 9–17 (2011).
53. Demin, A. & Tsiakaras, P. Thermodynamic analysis of a hydrogen fed solid oxide fuel cell based on a proton conductor. *Int. J. Hydrog. Energy* **26**, 1103–1108 (2001).
54. Han, D., Toyoura, K. & Uda, T. Protonated BaZr0. 8Y0. 2O3− δ: impact of hydration on electrochemical conductivity and local crystal structure. *ACS Appl. Energy Mater.* **4**, 1666–1676 (2021).

55. Lagaeva, J., Medvedev, D., Demin, A. & Tsiakaras, P. Insights on thermal and transport features of BaCe0. 8− xZrxY0. 2O3− δ proton-conducting materials. *J. Power Sources* **278**, 436–444 (2015).
56. Zhang, C. & Zhao, H. Electrical conduction behavior of Sr substituted proton conductor Ba1− xSrxCe0. 9Nd0. 1O3− δ. *Solid State Ion.* **181**, 1478–1485 (2010).
57. Kato, K., Han, D. & Uda, T. Transport properties of proton conductive Y-doped BaHfO3 and Ca or Sr-substituted Y-doped BaZrO3. *J. Am. Ceram. Soc.* **102**, 1201–1210 (2019).
58. Han, D. & Uda, T. The best composition of an Y-doped BaZrO 3 electrolyte: selection criteria from transport properties, microstructure, and phase behavior. *J. Mater. Chem. A.* **6**, 18571–18582 (2018).
59. Duan, C., Huang, J., Sullivan, N. & O'Hayre, R. Proton-conducting oxides for energy conversion and storage. *Appl. Phys. Rev.* **7**, 011314 (2020).
60. Zhu, H., Ricote, S., Duan, C., O'Hayre, R. P. & Kee, R. J. Defect chemistry and transport within dense BaCe0. 7Zr0. 1Y0. 1Yb0. 1O3− δ (BCZYYb) proton-conducting membranes. *J. Electrochem. Soc.* **165**, F845 (2018).
61. Zhu, H. et al. Defect incorporation and transport within dense BaZr0. 8Y0. 2O3− δ (BZY20) proton-conducting membranes. *J. Electrochem. Soc.* **165**, F581 (2018).
62. Duan, C. et al. Highly efficient reversible protonic ceramic electrochemical cells for power generation and fuel production. *Nat. Energy* **4**, 230–240 (2019).
63. Choi, S., Davenport, T. C. & Haile, S. M. Protonic ceramic electrochemical cells for hydrogen production and electricity generation: exceptional reversibility, stability, and demonstrated faradaic efficiency. *Energy Environ. Sci.* **12**, 206–215 (2019).
64. Choi, J., Shin, M., Kim, B. & Park, J.-S. High-performance ceramic composite electrodes for electrochemical hydrogen pump using protonic ceramics. *Int. J. Hydrog. Energy* **42**, 13092–13098 (2017).
65. Vøllestad, E. et al. Mixed proton and electron conducting double perovskite anodes for stable and efficient tubular proton ceramic electrolysers. *Nat. Mater.* **18**, 752–759 (2019).
66. Li, W., Guan, B., Ma, L., Tian, H. & Liu, X. Synergistic coupling of proton conductors BaZr0. 1Ce0. 7Y0. 1Yb0. 1O3− δ and La2Ce2O7 to create chemical stable, interface active electrolyte for steam electrolysis cells. *ACS Appl. Mater. Interfaces* **11**, 18323–18330 (2019).
67. Wrubel, J. A. et al. Modeling the performance and faradaic efficiency of solid oxide electrolysis cells using doped barium zirconate perovskite electrolytes. *Int. J. Hydrog. Energy* **46**, 11511–11522 (2021).
68. Sun, W., Shi, Z., Wang, Z. & Liu, W. Bilayered BaZr0. 1Ce0. 7Y0. 2O3-δ/Ce0. 8Sm0. 2O2-δ electrolyte membranes for solid oxide fuel cells with high open circuit voltages. *J. Membr. Sci.* **476**, 394–398 (2015).
69. Cao, J., Gong, Z., Hou, J., Cao, J. & Liu, W. Novel reduction-resistant Ba (Ce, Zr) 1− xGdxO3− δ electron-blocking layer for Gd0. 1Ce0. 9O2− δ electrolyte in IT-SOFCs. *Ceram. Int.* **41**, 6824–6830 (2015).
70. Prakash, B. S., Pavitra, R., Kumar, S. S. & Aruna, S. T. Electrolyte bi-layering strategy to improve the performance of an intermediate temperature solid oxide fuel cell: a review. *J. Power Sources* **381**, 136–155 (2018).
71. Wang, Z. et al. Preparation and performance of solid oxide fuel cells with YSZ/SDC bilayer electrolyte. *Ceram. Int.* **41**, 4410–4415 (2015).
72. Jiang, S. P. Nanoscale and nano-structured electrodes of solid oxide fuel cells by infiltration: advances and challenges. *Int. J. Hydrog. Energy* **37**, 449–470 (2012).
73. Rashkeev, S. N. & Glazoff, M. V. Atomic-scale mechanisms of oxygen electrode delamination in solid oxide electrolyzer cells. *Int. J. Hydrog. Energy* **37**, 1280–1291 (2012).
74. Nikolla, E., Schwank, J. & Linic, S. Promotion of the long-term stability of reforming Ni catalysts by surface alloying. *J. Catal.* **250**, 85–93 (2007).
75. Galea, N. M., Knapp, D. & Ziegler, T. Density functional theory studies of methane dissociation on anode catalysts in solid-oxide fuel cells: Suggestions for coke reduction. *J. Catal.* **247**, 20–33 (2007).
76. Raja, N., Murali, D., Posselt, M. & Satyanarayana, S. V. M. High temperature stability of BaZrO3: an ab initio thermodynamic study. *Phys. Status Solidi* **255**, 1700398 (2018).
77. Ribeiro, F. N. et al. Ab initio atomistic description of temperature-induced phase changes: the cases of zirconia and Ti-Y-co-doped zirconia. *Phys. Rev. Mater.* **5**, 023603 (2021).
78. Weng, M. H. et al. Kinetics and mechanisms for the adsorption, dissociation, and diffusion of hydrogen in Ni and Ni/YSZ slabs: a DFT study. *Langmuir* **28**, 5596–5605 (2012).
79. Bhatia, B. & Sholl, D. S. Chemisorption and diffusion of hydrogen on surface and subsurface sites of flat and stepped nickel surfaces. **122**, 204707 (American Institute of Physics, 2005).
80. Jing, Y., Matsumoto, H. & Aluru, N. R. Mechanistic insights into hydration of solid oxides. *Chem. Mater.* **30**, 138–144 (2018).
81. Klarbring, J., Vekilova, O. Y., Nilsson, J. O., Skorodumova, N. V. & Simak, S. I. Ionic conductivity in Sm-doped ceria from first-principles non-equilibrium molecular dynamics. *Solid State Ion.* **296**, 47–53 (2016).
82. Andersson, D. A., Simak, S. I., Skorodumova, N. V., Abrikosov, I. A. & Johansson, B. Optimization of ionic conductivity in doped ceria. *Proc. Natl Acad. Sci.* **103**, 3518–3521 (2006).
83. Ismail, A., Hooper, J., Giorgi, J. B. & Woo, T. K. A DFT+ U study of defect association and oxygen migration in samarium-doped ceria. *Phys. Chem. Chem. Phys.* **13**, 6116–6124 (2011).
84. Fronzi, M., Tateyama, Y., Marzari, N., Nolan, M. & Traversa, E. First-principles molecular dynamics simulations of proton diffusion in cubic BaZrO 3 perovskite under strain conditions. *Mater. Renew. Sustain. Energy* **5**, 14 (2016).
85. Zhu, K. et al. Engineering oxygen vacancy to accelerate proton conduction in Y-doped BaZrO3. *Ceram. Int.* **49**, 13321–13329 (2023).
86. Jacobs, R. et al. Unconventional highly active and stable oxygen reduction catalysts informed by computational design strategies. *Adv. Energy Mater.* **12**, 2201203 (2022).
87. Cadi-Essadek, A., Roldan, A. & De Leeuw, N. H. Stability and mobility of supported Ni n (n= 1–10) clusters on ZrO 2 (111) and YSZ (111) surfaces: a density functional theory study. *Faraday Discuss.* **208**, 87–104 (2018).
88. Ingram, D. B. & Linic, S. First-principles analysis of the activity of transition and noble metals in the direct utilization of hydrocarbon fuels at solid oxide fuel cell operating conditions. *J. Electrochem. Soc.* **156**, B1457 (2009).
89. Muñoz-García, A. B., Tuccillo, M. & Pavone, M. Computational design of cobalt-free mixed proton–electron conductors for solid oxide electrochemical cells. *J. Mater. Chem. A.* **5**, 11825–11833 (2017).
90. Lee, Y.-L., Kleis, J., Rossmeisl, J., Shao-Horn, Y. & Morgan, D. Prediction of solid oxide fuel cell cathode activity with first-principles descriptors. *Energy Environ. Sci.* **4**, 3966–3970 (2011).
91. Hong, W. T. et al. Toward the rational design of non-precious transition metal oxides for oxygen electrocatalysis. *Energy Environ. Sci.* **8**, 1404–1427 (2015).
92. Montoya, J. H., Doyle, A. D., Nørskov, J. K. & Vojvodic, A. Trends in adsorption of electrocatalytic water splitting intermediates on cubic ABO 3 oxides. *Phys. Chem. Chem. Phys.* **20**, 3813–3818 (2018).
93. Lee, Y.-L., Gadre, M. J., Shao-Horn, Y. & Morgan, D. Ab initio GGA+ U study of oxygen evolution and oxygen reduction electrocatalysis on the (001) surfaces of lanthanum transition metal perovskites LaBO 3 (B= Cr, Mn, Fe, Co and Ni). *Phys. Chem. Chem. Phys.* **17**, 21643–21663 (2015).
94. Grimaud, A. et al. Double perovskites as a family of highly active catalysts for oxygen evolution in alkaline solution. *Nat. Commun.* **4**, 2439 (2013).
95. Choi, Y., Lin, Me. C. & Liu, M. Computational study on the catalytic mechanism of oxygen reduction on La0. 5Sr0. 5MnO3 in solid oxide fuel cells. *Angew. Chem. Int. Ed.* **46**, 7214–7219 (2007).
96. Jacobs, R., Hwang, J., Shao-Horn, Y. & Morgan, D. Assessing correlations of perovskite catalytic performance with electronic structure descriptors. *Chem. Mater.* **31**, 785–797 (2019).
97. Tao, Z., Xu, X. & Bi, L. Density functional theory calculations for cathode materials of proton-conducting solid oxide fuel cells: a mini-review. *Electrochem. Commun.* **129**, 107072 (2021).
98. Bjørheim, T. S., Arrigoni, M., Saeed, S. W., Kotomin, E. & Maier, J. Surface segregation entropy of protons and oxygen vacancies in BaZrO3. *Chem. Mater.* **28**, 1363–1368 (2016).
99. Bjørheim, T. S., Kotomin, E. A. & Maier, J. Hydration entropy of BaZrO 3 from first principles phonon calculations. *J. Mater. Chem. A.* **3**, 7639–7648 (2015).
100. Bjørheim, T. S., Arrigoni, M., Gryaznov, D., Kotomin, E. & Maier, J. Thermodynamic properties of neutral and charged oxygen vacancies in BaZrO 3 based on first principles phonon calculations. *Phys. Chem. Chem. Phys.* **17**, 20765–20774 (2015).
101. Björketun, M. E., Sundell, P. G. & Wahnström, G. Structure and thermodynamic stability of hydrogen interstitials in BaZrO 3 perovskite oxide from density functional calculations. *Faraday Discuss.* **134**, 247–265 (2007).
102. Takahashi, H. et al. First-principles calculations for the energetics of the hydration reaction of acceptor-doped BaZrO3. *Chem. Mater.* **29**, 1518–1526 (2017).
103. Lee, Y.-L. et al. Defect thermodynamics and transport properties of proton conducting oxide $BaZr_{1-x}Y_xO_{3-\delta}$ ($x \le 0.1$) guided by density functional theory modeling. *JOM* **74**, 4506–4526 (2022).
104. Ding, H. & Hu, J. Degradation of carbamazepine by UVA/WO3/hypochlorite process: Kinetic modelling, water matrix effects, and density functional theory calculations. *Environ. Res.* **201**, 111569 (2021).
105. Xu, Z. et al. Revealing generation, migration, and dissociation of electron-hole pairs and current emergence in an organic photovoltaic cell. *Sci. Adv.* **7**, eabf7672 (2021).
106. Jain, A. et al. A high-throughput infrastructure for density functional theory calculations. *Comput. Mater. Sci.* **50**, 2295–2310 (2011).
107. Jain, A. et al. Commentary: the Materials Project: a materials genome approach to accelerating materials innovation. *APL Mater.* **1**, 011002 (2013).

108. Islam, M. S., Wang, S., Hall, A. T. & Mo, Y. First-principles computational design and discovery of solid-oxide proton conductors. *Chem. Mater.* **34**, 5938–5948 (2022).
109. Zhu, Y., He, X. & Mo, Y. Origin of outstanding stability in the lithium solid electrolyte materials: insights from thermodynamic analyses based on first-principles calculations. *ACS Appl. Mater. Interfaces* **7**, 23685–23693 (2015).
110. Chang, K.-S., Lin, Y.-F. & Tung, K.-L. Insight into the grain boundary effect on the ionic transport of yttria-stabilized zirconia at elevated temperatures from a molecular modeling perspective. *J. Power Sources* **196**, 9322–9330 (2011).
111. Fisher, C. A. J. & Matsubara, H. Oxide ion diffusion along grain boundaries in zirconia: a molecular dynamics study. *Solid State Ion.* **113**, 311–318 (1998).
112. Fisher, C. A. J. & Matsubara, H. Molecular dynamics investigations of grain boundary phenomena in cubic zirconia. *Comput. Mater. Sci.* **14**, 177–184 (1999).
113. Fisher, C. A. J. & Matsubara, H. The influence of grain boundary misorientation on ionic conductivity in YSZ. *J. Eur. Ceram. Soc.* **19**, 703–707 (1999).
114. González-Romero, R. L., Meléndez, J. J., Gómez-García, D., Cumbrera, F. L. & Domínguez-Rodríguez, A. A molecular Dynamics study of grain boundaries in YSZ: structure, energetics and diffusion of oxygen. *Solid State Ion.* **219**, 1–10 (2012).
115. Lee, H. B., Prinz, F. B. & Cai, W. Atomistic simulations of grain boundary segregation in nanocrystalline yttria-stabilized zirconia and gadolinia-doped ceria solid oxide electrolytes. *Acta Mater.* **61**, 3872–3887 (2013).
116. González-Romero, R. L., Meléndez, J. J., Gómez-García, D., Cumbrera, F. L. & Domínguez-Rodríguez, A. Segregation to the grain boundaries in YSZ bicrystals: a molecular dynamics study. *Solid State Ion.* **237**, 8–15 (2013).
117. An, J. et al. Atomic scale verification of oxide-ion vacancy distribution near a single grain boundary in YSZ. *Sci. Rep.* **3**, 1–6 (2013).
118. Huang, H. C., Su, P. C., Kwak, S. K., Pornprasertsuk, R. & Yoon, Y. J. Molecular dynamics simulation of oxygen ion diffusion in yttria stabilized zirconia single crystals and bicrystals. *Fuel Cells* **14**, 574–580 (2014).
119. Madrid, J. C. M., Matsuda, J., Leonard, K., Matsumoto, H. & Ghuman, K. K. Molecular dynamics study of oxygen-ion diffusion in yttria-stabilized zirconia grain boundaries. *J. Mater. Chem. A.* **10**, 2567–2579 (2022).
120. Devanathan, R., Weber, W. J., Singhal, S. C. & Gale, J. D. Computer simulation of defects and oxygen transport in yttria-stabilized zirconia. *Solid State Ion.* **177**, 1251–1258 (2006).
121. Kilo, M., Argirusis, C., Borchardt, G. & Jackson, R. A. Oxygen diffusion in yttria stabilised zirconia—experimental results and molecular dynamics calculations. *Phys. Chem. Chem. Phys.* **5**, 2219–2224 (2003).
122. Araki, W. & Arai, Y. Molecular dynamics study on oxygen diffusion in yttria-stabilized zirconia subjected to uniaxial stress in terms of yttria concentration and stress direction. *Solid State Ion.* **181**, 1534–1541 (2010).
123. Shimojo, F., Okabe, T., Tachibana, F., Kobayashi, M. & Okazaki, H. Molecular dynamics studies of yttria stabilized zirconia. I. Structure and oxygen diffusion. *J. Phys. Soc. Jpn.* **61**, 2848–2857 (1992).
124. Shimojo, F. & Okazaki, H. Molecular dynamics studies of yttria stabilized zirconia. II. Microscopic mechanism of oxygen diffusion. *J. Phys. Soc. Jpn.* **61**, 4106–4118 (1992).
125. Ogawa, H., Sawaguchi, N. & Wakai, F. High temperature deformation of ceramics simulated by molecular dynamics. *Mater. Sci. Forum* **243-245**, 351–356 (1996).
126. Chang, K. S. & Tung, K. L. Oxygen-ion transport in a dual-phase scandia–yttria-stabilized zirconia solid electrolyte: a molecular dynamics simulation. *ChemPhysChem* **10**, 1887–1894 (2009).
127. Van Duin, A. C. T., Dasgupta, S., Lorant, F. & Goddard, W. A. ReaxFF: a reactive force field for hydrocarbons. *J. Phys. Chem. A* **105**, 9396–9409 (2001).
128. Van Duin, A. C. T., Merinov, B. V., Han, S. S., Dorso, C. O. & Goddard Iii, W. A. ReaxFF reactive force field for the Y-doped BaZrO3 proton conductor with applications to diffusion rates for multigranular systems. *J. Phys. Chem. A* **112**, 11414–11422 (2008).
129. Cammarata, A., Emanuele, A. & Duca, D. Y: BaZrO3 perovskite compounds II: designing protonic conduction by using MD models. *Chem. Asian J.* **7**, 1838–1844 (2012).
130. Li, X., Zhang, L., Tang, Z. & Liu, M. Fast oxygen transport in bottlelike channels for Y-doped BaZrO3: a reactive molecular dynamics investigation. *J. Phys. Chem. C.* **123**, 25611–25617 (2019).
131. Ottochian, A. et al. Influence of isotropic and biaxial strain on proton conduction in Y-doped BaZrO 3: a reactive molecular dynamics study. *J. Mater. Chem. A.* **2**, 3127–3133 (2014).
132. Merinov, B., Duin, A. V., Haile, S. & Goddard Iii, W. A. Reactive force fields for y-doped BaZrO3 electrolyte and ni-anode. potential cathode materials for application in proton ceramic fuel cells. (California Institute of Technology (US), 2004).
133. Hossain, M. K. et al. A review on experimental and theoretical studies of perovskite barium zirconate proton conductors. *Emergent Mater.* **4**, 999–1027 (2021).
134. Bedrov, D., Smith, G. D. & van Duin, A. C. T. Reactions of singly-reduced ethylene carbonate in lithium battery electrolytes: a molecular dynamics simulation study using the ReaxFF. *J. Phys. Chem. A* **116**, 2978–2985 (2012).
135. Islam, M. M., Kolesov, G., Verstraelen, T., Kaxiras, E. & Van Duin, A. C. T. eReaxFF: a pseudoclassical treatment of explicit electrons within reactive force field simulations. *J. Chem. Theory Comput.* **12**, 3463–3472 (2016).
136. Islam, M. M. & Van Duin, A. C. T. Reductive decomposition reactions of ethylene carbonate by explicit electron transfer from lithium: an eReaxFF molecular dynamics study. *J. Phys. Chem. C.* **120**, 27128–27134 (2016).
137. Evangelisti, B., Fichthorn, K. A. & Van Duin, A. C. T. Development and initial applications of an e-ReaxFF description of Ag nanoclusters. *J. Chem. Phys.* **153**, 104106 (2020).
138. Akbarian, D., Ganeshan, K., Woodward, W. H. H., Moore, J. & Van Duin, A. C. T. Atomistic-scale insight into the polyethylene electrical breakdown: an eReaxFF molecular dynamics study. *J. Chem. Phys.* **154**, 024904 (2021).
139. Te Velde, G. T. et al. Chemistry with ADF. *J. Comput. Chem.* **22**, 931–967 (2001).
140. Verdi, C., Karsai, F., Liu, P., Jinnouchi, R. & Kresse, G. Thermal transport and phase transitions of zirconia by on-the-fly machine-learned interatomic potentials. *NPJ Comput. Mater.* **7**, 156 (2021).
141. Guan, S.-H., Shang, C. & Liu, Z.-P. Resolving the temperature and composition dependence of ion conductivity for yttria-stabilized zirconia from machine learning simulation. *J. Phys. Chem. C.* **124**, 15085–15093 (2020).
142. Guan, S.-H., Zhang, K.-X., Shang, C. & Liu, Z.-P. Stability and anion diffusion kinetics of Yttria-stabilized zirconia resolved from machine learning global potential energy surface exploration. *J. Chem. Phys.* **152**, 094703 (2020).
143. Wang, Z. et al. A machine-learning interatomic potential to understand the anisotropic fracture behavior of Bazro3 material. Available at SSRN 4419876. https://doi.org/10.2139/ssrn.4419876.
144. Niu, H. et al. On the anomalous diffusion of proton in Y-doped BaZrO3 perovskite oxide. *Solid State Ion.* **376**, 115859 (2022).
145. Kholtobina, A. S., Forslund, A., Ruban, A. V., Johansson, B. & Skorodumova, N. V. Temperature dependence of (111) and (110) ceria surface energy. *Phys. Rev. B* **107**, 035407 (2023).
146. Modak, A. U. & Lusk, M. T. Kinetic Monte Carlo simulation of a solid-oxide fuel cell: I. open-circuit voltage and double layer structure. *Solid State Ion.* **176**, 2181–2191 (2005).
147. Pornprasertsuk, R., Ramanarayanan, P., Musgrave, C. B. & Prinz, F. B. Predicting ionic conductivity of solid oxide fuel cell electrolyte from first principles. *J. Appl. Phys.* **98**, 103513 (2005).
148. Pornprasertsuk, R., Cheng, J., Huang, H. & Prinz, F. B. Electrochemical impedance analysis of solid oxide fuel cell electrolyte using kinetic Monte Carlo technique. *Solid State Ion.* **178**, 195–205 (2007).
149. Wang, X., Lau, K. C., Turner, C. H. & Dunlap, B. I. Kinetic Monte Carlo simulation of the elementary electrochemistry in a hydrogen-powered solid oxide fuel cell. *J. Power Sources* **195**, 4177–4184 (2010).
150. Krishnamurthy, R., Yoon, Y. G., Srolovitz, D. J. & Car, R. Oxygen diffusion in yttria-stabilized zirconia: a new simulation model. *J. Am. Ceram. Soc.* **87**, 1821–1830 (2004).
151. Dholabhai, P. P., Anwar, S., Adams, J. B., Crozier, P. A. & Sharma, R. Predicting the optimal dopant concentration in gadolinium doped ceria: a kinetic lattice Monte Carlo approach. *Modell. Simul. Mater. Sci. Eng.* **20**, 015004 (2011).
152. Gunn, D. S. D., Purton, J. A. & Metz, S. Monte Carlo simulations of gadolinium doped ceria surfaces. *Solid State Ion.* **324**, 128–137 (2018).
153. Zhang, Y., Ni, M., Yan, M. & Chen, F. Thermal aging stability of infiltrated solid oxide fuel cell electrode microstructures: a three-dimensional kinetic Monte Carlo simulation. *J. Power Sources* **299**, 578–586 (2015).
154. Eisele, S., Draber, F. M. & Grieshammer, S. The effect of ionic defect interactions on the hydration of yttrium-doped barium zirconate. *Phys. Chem. Chem. Phys.* **23**, 4882–4891 (2021).
155. Gomez, M. A., Fry, D. L. & Sweet, M. E. Effects on the proton conduction limiting barriers and trajectories in BaZr 0.875 Y 0.125 O 3 due to the presence of other protons. *J. Korean Ceram. Soc.* **53**, 521–528 (2016).
156. Yamazaki, Y. et al. Proton trapping in yttrium-doped barium zirconate. *Nat. Mater.* **12**, 647–651 (2013).
157. Ma, L., Priya, P. & Aluru, N. R. A multiscale model for electrochemical reactions in LSCF based solid oxide cells. *J. Electrochem. Soc.* **165**, F1232 (2018).
158. Asproulis, N., Kalweit, M., Shapiro, E. & Drikakis, D. Mesoscale flow and heat transfer modelling and its application to liquid and gas flows. *J. Nanophotonics* **3**, 031960 (2009).
159. Ren, B., Li, J., Wen, G., Ricardez− Sandoval, L. & Croiset, E. First-principles based microkinetic modeling of CO2 reduction at the Ni/SDC cathode of a solid oxide electrolysis cell. *J. Phys. Chem. C.* **122**, 21151–21161 (2018).
160. Khaleel, M. A., Rector, D. R., Lin, Z., Johnson, K. & Recknagle, K. Multiscale electrochemistry modeling of solid oxide fuel cells. *Int. J. Multiscale Comput. Eng.* **3**, 33–48 (2005).

161. Cheng, C. H., Chang, Y. W. & Hong, C. W. Multiscale parametric studies on the transport phenomenon of a solid oxide fuel cell. *J. Fuel Cell Sci. Technol.* **2**, 219 (2005).
162. Pasaogullari, U. & Wang, C.-Y. Computational fluid dynamics modeling of solid oxide fuel cells. *ECS Proc. Vol.* **2003**, 1403 (2003).
163. Andersson, M., Yuan, J. & Sundén, B. Review on modeling development for multiscale chemical reactions coupled transport phenomena in solid oxide fuel cells. *Appl. Energy* **87**, 1461–1476 (2010).
164. Li, Z., Zhang, H., Xu, H. & Xuan, J. Advancing the multiscale understanding on solid oxide electrolysis cells via modelling approaches: a review. *Renew. Sustain. Energy Rev.* **141**, 110863 (2021).
165. Janardhanan, V. M. & Deutschmann, O. CFD analysis of a solid oxide fuel cell with internal reforming: coupled interactions of transport, heterogeneous catalysis and electrochemical processes. *J. Power Sources* **162**, 1192–1202 (2006).
166. Karakasidis, T. E. & Charitidis, C. A. Multiscale modeling in nanomaterials science. *Mater. Sci. Eng. C.* **27**, 1082–1089 (2007).
167. Frayret, C., Villesuzanne, A., Pouchard, M. & Matar, S. Density functional theory calculations on microscopic aspects of oxygen diffusion in ceria-based materials. *Int. J. Quantum Chem.* **101**, 826–839 (2005).

ACKNOWLEDGEMENTS

Work supported through the INL Laboratory Directed Research& Development (LDRD) Program under DOE Idaho Operations Office Contract DE-AC07-05ID14517.

AUTHOR CONTRIBUTIONS

P.G. and G.P. conceived the idea and developed the manuscript outline. G.P. led the collaboration. P.G. wrote a major part of the manuscript. All authors (P.G., K.M., Y.S., A.V.D., and G.P.) reviewed and edited the manuscript.

COMPETING INTERESTS

The authors declare no competing interests.

ADDITIONAL INFORMATION

Correspondence and requests for materials should be addressed to Gorakh Pawar.

Reprints and permission information is available at http://www.nature.com/reprints

Publisher's note Springer Nature remains neutral with regard to jurisdictional claims in published maps and institutional affiliations.